Title

STUDY OF n- + p --> n- + n+ AT 1.25 AND 1.75 BeV/c FOR LOW-NUCLEON-MOMENTUM-TRANSFER COLLISIONS: EVIDENCE FOR PION-PION INTERACTIONS

Author

Johnson, William Brule.

Publication Date

1963-02-27

University of California

Ernest O. Lawrence Radiation Laboratory

STUDY OF

$\pi^- + p \longrightarrow \pi^- + \pi^+ + n$ at 1.25 and 1.75 BeV/c FOR LOW-NUCLEON-MOMENTUM-TRANSFER COLLISIONS: EVIDENCE FOR PION-PION INTERACTIONS

Berkeley, California

DISCLAIMER

UCRL-10703
UC-34 Physics
TID-4500 (18th Ed.)

UNIVERSITY OF CALIFORNIA

Lawrence Radiation Laboratory
Berkeley, California

Contract No. W-7405-eng-48

STUDY OF $\pi^- + p \rightarrow \pi^- + \pi^+ + n$ AT 1.25 AND 1.75 BeV/c FOR LOW-NUCLEON-MOMENTUM-TRANSFER COLLISIONS: EVIDENCE FOR PION-PION INTERACTIONS

William Brulé Johnson

(Ph. D. Thesis)

February 27, 1963

Printed in USA. Price $2.25. Available from the
Office of Technical Services
U. S. Department of Commerce
Washington 25, D.C.

STUDY OF $\pi^- + p \rightarrow \pi^- + \pi^+ + n$ AT 1.25 AND 1.75 BeV/c FOR LOW-NUCLEON-MOMENTUM-TRANSFER COLLISIONS: EVIDENCE FOR PION-PION INTERACTIONS

Contents

STUDY OF $\pi^- + p \rightarrow \pi^- + \pi^+ + n$ AT 1.25 AND 1.75 BeV/c FOR LOW-NUCLEON-MOMENTUM-TRANSFER COLLISIONS: EVIDENCE FOR PION-PION INTERACTIONS

William Brulé Johnson

Lawrence Radiation Laboratory
University of California
Berkeley, California

February 27, 1963

ABSTRACT

We studied the process $\pi^- p \rightarrow \pi^- \pi^+ n$ at incident pion momenta of 1.25 and 1.75 BeV/c. Two arrays of plastic scintillation counters were used to detect the final-state particles: the first array--15 cm thick, and 160 cm from the liquid-hydrogen target where the interaction occurred--detected both pions and neutrons in the forward π steradians; a second array of thin scintillators, placed near the hydrogen target, was used to detect pions in the remaining angular region. The energy of the neutron was determined by measuring its flight time from the liquid hydrogen target to the first array. Only neutrons from 5 to 65 MeV were detected, thus limiting our study to those collisions in which the four-momentum transfer squared from the proton to the neutron was less than 6.5 μ^2 (where μ is the mass of the pion).

Study of the data as a function of the "mass" of the two-pion final-state system corroborates the presence of a pion-pion resonance at a mass value of 750 MeV. The width of the resonance is somewhat greater than that found in experiments dealing with other charge states.

We attempt to extract pion-pion total cross sections from the data by the Chew-Low extrapolation method. The results obtained are physically untenable and indicate failure of the extrapolation method when applied to these data.

Considerable evidence is found for final-state interaction between the neutron and one of the pions. The data are subjected to the Treiman-Yang test to discover any deviations from the one-pion-exchange model; considerable deviation is found for large momentum-transfer collisions.

It is felt that the large resonance width and the failure of the Chew-Low extrapolation method are results of final-state interactions not accounted for in the one-pion-exchange model.

I. INTRODUCTION

In 1959 Chew and Low proposed a method[1] for obtaining pion-pion cross sections from the study of the process

$$\pi + N \rightarrow \pi + \pi + N . \tag{I-1}$$

Let us establish the following notation: μ and $(\vec{q}_{1L}, \omega_{1L})$ are the mass and laboratory-system four-momentum of the incident meson; M_1 is the mass of the target nucleon; μ_1 and $(\vec{p}_{\pi 1}, \omega_{\pi 1})$ are the mass and laboratory-system four-momentum of the first pion in the final state; μ_2 and $(\vec{p}_{\pi 2}, \omega_{\pi 2})$ are the mass and laboratory-system four-momentum of the second final-state pion; and M_2 and $(\vec{p}_2, \omega_2)$ are the mass and laboratory-system four momentum of the final-state nucleon. Further let us define three Lorentz-invariant quantities:

$$w^2 = (\omega_{1L} + M_1 - \omega_2)^2 - q_{1L}^2 - p_2^2 + 2q_{1L}p_2\cos\theta_2, \tag{I-2}$$

$$\Delta^2 = -(\omega_2 - M_1)^2 + p_2^2 = 2M_1T_2 - (M_1 - M_2)^2 ,$$

and

$$p^2 = (M_2/M_1)\left[\Delta^2 + (M_1 - M_2)^2\right] = 2M_2T_2 ,$$

where θ_2 is defined by

$$\cos\theta_2 = \frac{\vec{q}_{1L}}{q_{1L}} \cdot \frac{\vec{p}_2}{p_2} \tag{I-3}$$

and T_2 is the laboratory-system kinetic energy of the final-state neutron. From four-momentum conservation we can rewrite w^2 as

$$w^2 = (\omega_{\pi 1} + \omega_{\pi 2})^2 - (p_{\pi 1} + p_{\pi 2})^2;$$

apparently w is the total energy of the two final-state pions in their own barycentric frame--the so-called "invariant mass" of the two-pion system.

In terms of Feynman diagrams Chew and Low proposed that the one-pion-exchange graph (see Fig. 1) dominated the interaction given in Eq. (I-1) in the region of low momentum transfers, Δ^2. They justified

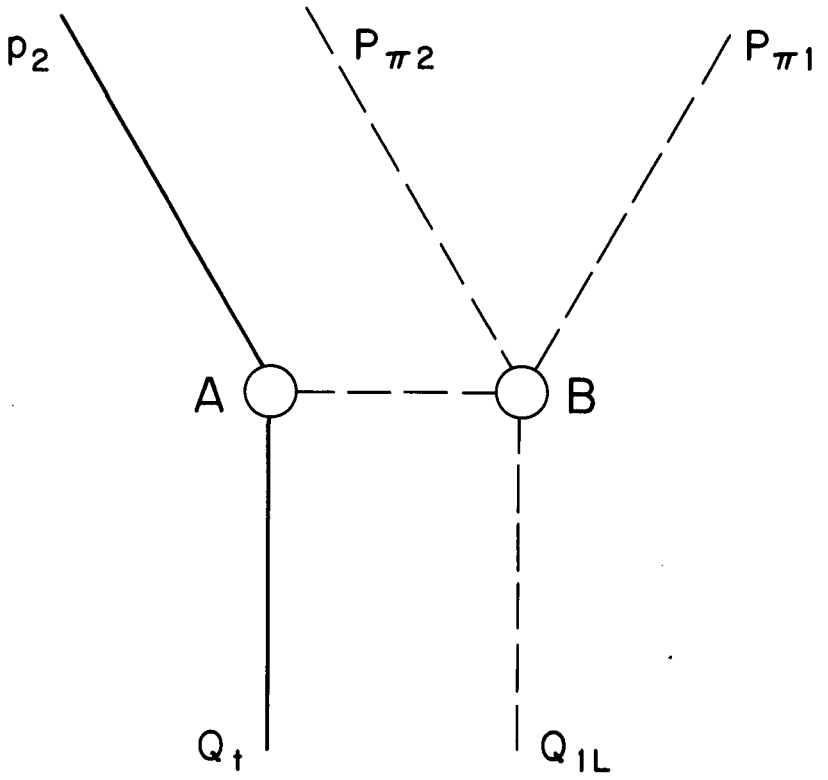

Fig. 1. Feynman graph depicting the one-pion-exchange process in pion production by pions.

this proposal by pointing out the analyticity properties of the amplitude in the variable Δ^2. It is well known from the structure of the Feynman graphs that the transmission of a virtual particle from vertex A to vertex B introduces into the amplitude a denominator $\Delta^2 + m^2$ (where m is the mass of the particle transmitted). This denominator contributes a simple pole to the amplitude in the nonphysical region of the variable Δ^2 at the point $\Delta^2 = - m^2$. Since the pion is the lightest particle with quantum numbers appropriate for connecting vertices A and B, the singularity in the one-pion-exchange graph is nearest the physical region of the variable Δ^2; graphs that exchange more massive systems introduce singularities more remote from the physical region and hence contribute slowly varying functions of Δ^2 to the amplitude in the region of low momentum transfer. Conservation of G parity requires exchange of an odd number of pions[2] between A and B; therefore the next nearest singularity results from three-pion exchange. Since the three-pion system may have some internal motion, the mass is not fixed; the singularity introduced is a branch cut beginning at $\Delta^2 = - 9\mu^2$ and extending to the point at infinity. The branch point is thus removed nine times as far from the edge of the physical region as is the pole from one-pion exchange.

Chew and Low calculated the contribution to the cross section $d^2\sigma/d(p^2)d(w^2)$ from the one-pion-exchange process to be

$$\frac{d^2\sigma}{d(p^2)d(w^2)} = \frac{f^2}{2\pi q_{1L}^2} \frac{(p^2/\mu^2)}{(p^2-p_0^2)^2} \frac{M_2^2}{M_1^2} \left[\frac{w^4}{4} - \frac{w^2}{2}(\mu_1^2+\mu_2^2) + \frac{1}{4}(\mu_1^2-\mu_2^2)^2\right]^{1/2} \times \sigma_{12}(w^2), \qquad \text{(I-4)}$$

where $p_0^2 = (M_2/M_1)(-\mu^2 + (M_1 - M_2)^2$, and f^2 is the pion-nucleon coupling constant appropriate to the meson exchanged: $f^2 = f_0^2 \approx 0.08$ for a neutral pion crossing from vertex A to B or $f^2 = 2f_0^2$ for exchange of a charged pion. The quantity $\sigma_{12}(w^2)$ would be exactly the

physical pion-pion total cross section if the pion exchanged were on the mass shell--i.e., if $\omega_\pi^2 - p_\pi^2 = \mu^2$. This condition is fulfilled at the pole $\Delta^2 = -\mu^2$; apart from kinematical factors, the residue at this pole (which enters in second order into the cross section) is simply the pion-nucleon coupling constant f^2 times the physical pion-pion cross section. To implement these considerations with physical data, Chew and Low construct the function $F(p^2, w^2)$:

$$F(p^2, w^2) = 2\pi \frac{M_1^2}{M_2^2} \frac{q_{1L}^2 (p^2 - p_0^2)^2}{\left[\frac{w^4}{4} - \frac{w^2}{2}(\mu_1^2 + \mu_2^2) + \frac{1}{4}(\mu_1^2 - \mu_2^2)^2\right]^{1/2}} \frac{d^2\sigma}{d(p^2)d(w^2)} \tag{I-5}$$

The experimenter measures $d^2\sigma/d(p^2)d(w^2)$ at constant w^2 for several values of p^2, calculates the corresponding value of F, and attempts to extrapolate the data from the physical domain of p^2 to the nonphysical point p_0^2. The value of F at this point is

$$F(p_0^2, w^2) = -f^2 \sigma_{\pi\pi}(w^2) . \tag{I-6}$$

The success in strong interactions of the concept of isotopic spin[3] leads us to classify the two-pion system in terms of the three possible isotopic spin states $I = 0$, 1, and 2. Table I summarizes this information.

In 1961 several experimenters reported studying the processes

$$\pi^\pm + p \rightarrow \pi^\pm + \pi^0 + p . \tag{I-7}$$

Erwin et al.[4] included both final states, $(\pi^+\pi^- n)$ and $(\pi^-\pi^0 p)$. By integration of Eq. (I-4) over p^2, they obtained from the distributions in the physical region an average of $\sigma_{12}(w^2)$ over the final-state systems $(\pi^+\pi^-)$ and $(\pi^-\pi^0)$. Pickup et al.[5] studied reaction (I-7) in terms of the mass of the two-pion final-state system. Anderson et al.[6] reported two experiments with the processes (I-7) at two different incident momenta; they treated their data by the Chew-Low extrapolation method. The results of these experiments establish the existence of a pion-pion resonance

in the $I = 1$, $J = 1$ state, where I and J are the total isotopic spin and total angular momentum, respectively, of the two-pion system. The resonance occurs at $w = 750$ MeV and has a full width at one-half maximum of approximately 150 MeV. This resonant state is known in the literature as the ρ meson.

All the experiments described above were performed in hydrogen bubble chambers, which are well suited for a study of the low-energy recoil protons in the final state of reaction (I-7).

In the remainder of this paper we describe a study of the similar process

$$\pi^- + p \rightarrow \pi^- + \pi^+ + n \qquad \text{(I-8)}$$

performed with the Lawrence Radiation Laboratory Bevatron at two incident-pion momenta, 1.25 and 1.75 BeV/c. From Table I, we see that the $(\pi^+\pi^-)$ system contains all three isotopic spin states; a strong pion-pion interaction in any of the isotopic channels should be manifest in process (I-8). Inspection of Eq. (I-2) shows that both p^2 and w^2 can be derived from a knowledge of the laboratory-system energy and polar scattering angle of the neutron. Our experimental problem, therefore, is first to identify unambiguously the final-state system of process (I-8), then to measure as well as possible the neutron energy and scattering angle.

Sections II and III describe our treatment of these problems. Section IV presents the results of the study.

Table I. Decomposition of the two-pion system into isotopic spin components.

Two-pion system	Isotopic Composition		
	I = 0	I = 1	I = 2
$(\pi^+\pi^+)$	0	0	1
$(\pi^+\pi^0)$	0	1/2	1/2
$(\pi^+\pi^-)$	1/3	1/2	1/6
$(\pi^0\pi^0)$	1/3	0	2/3
$(\pi^-\pi^0)$	0	1/2	1/2
$(\pi^-\pi^-)$	0	0	1

II. EXPERIMENTAL APPARATUS AND TECHNIQUES

A. The Beam System

A secondary beam of negative pions was produced by bombarding a 2-in.-long beryllium target with the primary proton beam of the Bevatron. The target was positioned in the west tangent tank (one of the field-free straight sections of the Bevatron) so that particles produced at 32 deg with respect to the primary beam were accepted into a system of bending and strong-focusing magnets[7] (see Fig. 2). The field direction in the two bending magnets, M1 and M2, determined the charge of the secondary beam; the field setting in M2 defined the central momentum of the beam to ±4% and was calibrated by use of a wire-orbit technique.[8] The field gradients of the strong-focusing magnets Q1, Q2, Q3, Q4, and Q5 were selected to focus the secondary beam onto a liquid hydrogen target at the third focus of the system.

Particles passing down the beam channel were detected by three beam-monitoring counters, S1, C1, and S3. To reduce the effect of multiple scattering in these detectors, we placed them as close as possible to the three foci of the magnetic optical system. Counter S1 was a plastic scintillation counter 0.5 cm thick in the beam direction and 5.0 cm in diameter, C1 was a cyclohexene Cerenkov counter 7.6 cm long and 7.6 cm in diameter, and S3 was a thin plastic scintillator 0.1 cm thick and 7.0 cm in diameter. We made S3 as thin as possible to reduce the non-hydrogen-derived scattering of beam particles in the vicinity of the hydrogen target. The target itself presented to the beam (a) an entrance window of Mylar 0.030 in. thick, (b) 12 sheets of aluminized Mylar, each 0.0033 in. thick, used as a heat shield, (c) a hemispherically shaped, liquid hydrogen flask, made of 0.005-in. Mylar, 4 in. in radius with the flat side of the hemispheroid toward the incident beam, and (d) an aluminium exit dome 0.062 in. thick.

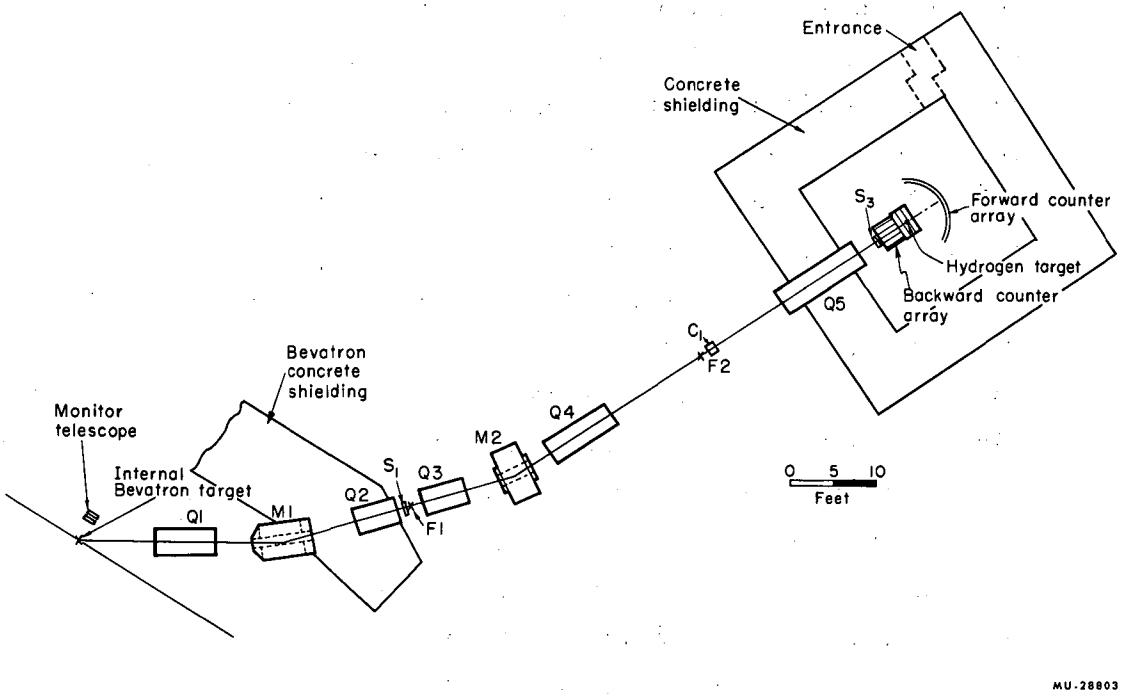

Fig. 2. Diagram of magnet system and counter placement.

A coincidence between the counters S1, C1, and S3--when set at the proper relative delay for pions--ensured that a particle of the correct momentum and charge had traversed the entire beam channel and had passed into the liquid hydrogen flask of the target.

To minimize multiple scattering along the path of the beam channel the whole system was threaded with polyethylene bags filled with helium.

We designed the beam channel and monitoring system to accommodate both positive and negative secondary beams, as several experiments were being performed with the same beam apparatus. Such versatility required that we place the primary target in a field-free region and extract a secondary beam at a large production angle; this resulted in a loss of intensity of negative beams. Further, with positive beams, it was necessary to distinguish between positive pions and protons; hence, we used the velocity-selecting Cerenkov counter, C1.

For central momenta as high as 1.25 and 1.75 BeV/c, the negative beams extracted along this beam channel were composed almost entirely of π mesons. The principal contamination in the beam consists of μ mesons and electrons; since these contaminants are not produced in strong interaction collisions, they must come from two major decay sources--decay processes in the vicinity of the primary target and pion and muon decays along the beam channel. For our system, a range curve, taken for a beam of negative particles with central momentum 280 MeV/c, indicated a contamination of approximately 10%. Because Lorentz time dilation inhibits decays along the beam channel, contamination decreases rapidly as one increases the momentum of the beam. A calculation similar to that described by Rogers[9] allows us to estimate our contamination as $3 \pm 3\%$ at 1.25 BeV/c and $2 \pm 2\%$ at 1.75 BeV/c.

Since muons and electrons do not interact strongly in hydrogen, their presence in the beam can affect our results by no more than an over-all normalization factor.

B. Detection of Final-State Particles

The apparatus for detecting the final-state particles of Eq. (I-8) consisted of two arrays of plastic scintillation counters.

Array I (see Fig. 3a and 3c) was composed of 84 counters shaped like trapezoidal prisms and deployed across a portion of the surface of a sphere. The sphere had a radius of 160 cm and was centered at the liquid hydrogen target. This array detected both neutrons and pions. To detect neutrons with appreciable efficiency, we made the 84 counters each 15 cm thick; a neutron, with kinetic energy between 5 and 65 MeV, traversing this thickness of plastic scintillator, had roughly a 25% probability of giving rise to detectable charged recoils by means of n-p elastic scattering or (at the high-energy end of this energy interval) by inelastic neutron-carbon scattering. In Sec. II-F we describe precise measurements of this detection efficiency.

The 84 counters of this array were grouped into seven intervals in polar angle, each with a full-width angular resolution of 8 deg. Each of these intervals (which appeared as concentric rings when viewed along the incident-beam direction, as shown in Fig. 3c) contained 12 counters and hence had a resolution of 30 deg in azimuthal angle. Array I covered the polar angular region completely from 4 deg to 60 deg, the 4-deg hole in the center serving as an exit for the incident beam.

Each of the 84 elements was connected by a hollow aluminum light guide to a separate photomultiplier tube. The three inner rings (whose elements were relatively small) were viewed by RCA 6810 tubes ($\approx$ 2 in. photocathode) and the outer four rings by RCA 7046 tubes ($\approx$ 4 in. photocathode). Each counter of this array was a totally separate lighttight unit.

Array II (see Fig. 3a and 3b) was a hodoscope device with 15 elements--12 elements parallel to the incident beam which were arranged axially about it like the staves of a barrel 58 cm long and 46 cm in diameter--and 3 elements (each containing two separate counters) exterior to the barrel and formed into hoops about it. The hoops covered

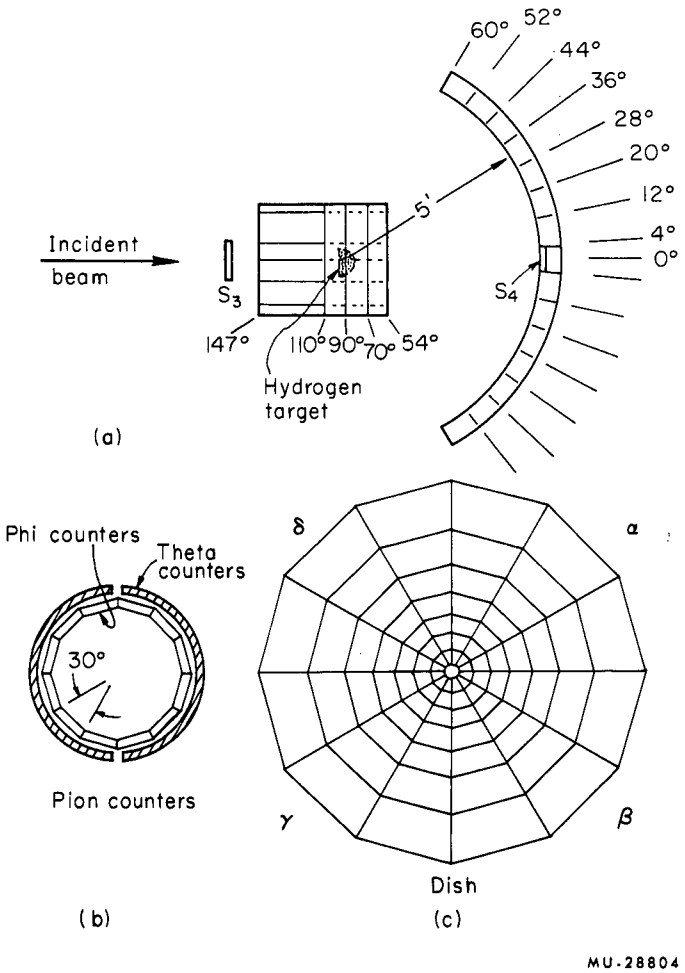

Fig. 3. Geometric arrangement of counters. The side view is shown in (a). Front views of Arrays II and I are shown separately in (b) and (c) as viewed along the incident beam.)

approximately three-quarters of the barrel; the remaining portion was uncovered. Used as a hodoscope, this device had an angular resolution of 30 deg in azimuth (the same aximuthal resolution as Array I), and approximately 20 deg in polar angle (four intervals in polar angle, the fourth interval being defined by a count recorded in the barrel staves but not recorded in the hoops). The counters in this array were 1.0-cm-thick plastic scintillators; unlike Array I they detected only final-state pions. The kinematics of process (I-8), with incident-pion momenta of 1.25 and 1.75 BeV/c, are such that one pion in the final state always has a polar angle less than 60 deg for spectator neutrons with energies between 5 and 65 MeV. Thus, Array II, which covered all polar angles from 60 to 150 deg, was required to detect only one of the final-state pions; thus, its hodoscope nature proved no restriction.

The final counter in the system, S4, was a plastic scintillator 1.0 cm thick and 21 cm in diameter; it was mounted in the 4-deg beam-exit hole in the center of Array I. This counter was placed in anti-coincidence with the beam-monitoring counters S1, C1, and S3. The signal T,

$$T = S1\ C1\ S3\ \overline{S4}\ , \qquad \text{(II-1)}$$

(where the bar signifies an anticoincidence) indicated that a beam particle had traversed the beam system, entered the liquid hydrogen target, and scattered through a polar angle greater than 4 deg.

C. The Electronic System

The photomultiplier outputs from Arrays I and II were standardized by use of tunnel diode discriminating circuits.[10] Whenever the peak voltage of the input signal was greater than a preset value, the discriminators produced a "standard" pulse with a height of approximately 60 mV and a width at the base of approx 7 nsec. Each circuit had two signal outputs to allow for timing and recording of particles detected by Array I. In effect, the timing signal, Σ, was obtained by summing onto a single channel one output from each of the discriminators for Array I.[11]

The electronic system that treated the signal outputs from these various devices (discriminators, counters, timing signals) consisted of three parts:[12] (a) a system of coincidence circuitry which, under appropriate logical conditions, generated a trigger pulse to activate the rest of the system; (b) a device known as the Chronotron for timing measurements; and (c) a data-storage and recording system. Figure 4 shows a simplified block diagram of these components.

A trigger was generated whenever an incident-beam particle was scattered in the liquid hydrogen target and a slow particle in Array I was detected 10 to 60 nsec later. To generate this trigger, the signal T produced a 50 nsec gate which, with the proper delay, was placed in coincidence with the timing signal Σ. An output from this coincidence did two things: first, it allowed the timing reference T and the signal-to-be-timed, Σ, to pass on to the Chronotron; second, it generated two gates, a fast gate 10 nsec wide and a slow gate 50 nsec wide, which activated the data-storage system.

The Chronotron[13] was a timing device which allowed us to measure the flight time of the final-state neutrons [of process (I-8)] from the liquid hydrogen target to Array I, a flight path of 160 cm. Such a measurement determined the energy of the neutron. The Chronotron compared the time of arrival of neutrons at Array I with the time of arrival of scattered pions ($\beta \approx 1$). The measurement was made for $\tau = t_n - t_\pi$ in the interval 11 nsec $\leq \tau \leq 46$ nsec (corresponding to a neutron-energy interval of approximately 5 to 65 MeV). This timing interval was divided into seven subintervals such that

$$\frac{\Delta\tau}{\tau} \approx \frac{2\Delta T_n}{T_n} \approx 0.15 \qquad \text{(II-2)}$$

was approximately constant, where T_n is the laboratory-system kinetic energy of the neutron. When a neutron was detected, the Chronotron selected the subinterval (or time bin, as it was called) that was appropriate to the time of flight and relayed this information to the data-storage equipment to be recorded with the other coordinates of the event.

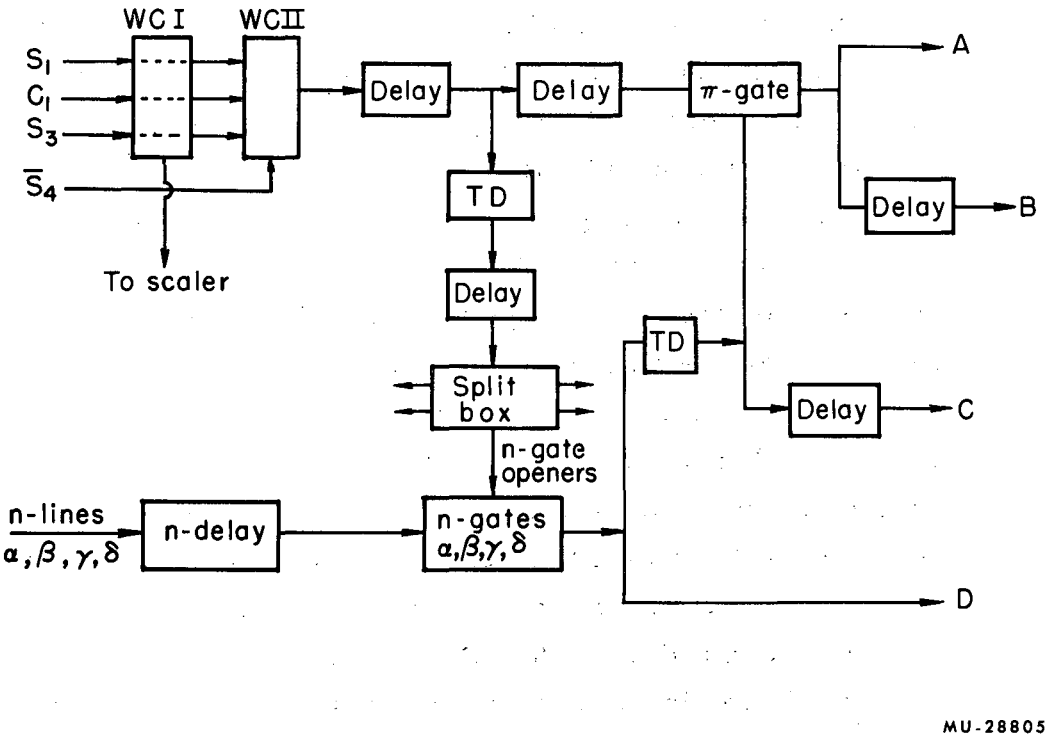

Fig. 4. Simplified block diagram of the electronics. From point A, the signal goes to the Chronotron, where it provides the zero reference time τ_0 corresponding to the flight time of a pion, with $\beta \approx 1$, between the target and Array I. From B the signal goes to gate-generator units which provide pulses that gate on the pion coincidence-discriminator circuits. From C, the neutron coincidence-discriminator circuits are gated on. From D, the signal goes to the Chronotron to give the neutron timing τ_n compared with the reference signal τ_0.

Table II summarizes the flight-time intervals associated with each time bin.

The outputs from all the elements in both Array I and Array II entered the data-storage system through individual two-channel coincidence circuits. These circuits gave an output whenever a pulse from one of the counters and a gate pulse generated by the trigger system overlapped temporally. The Array I outputs passed through two such coincidence circuits, the first driven by a gate in time with fast particles (i.e., pions) and the second driven by a gate in time with the slow particle detected. Array II outputs passed through units driven by the fast gate. The outputs were recorded in a set of flip-flops which in turn were transmitted to a magnetic-core storage buffer, which recorded the status of each counter in both counter arrays and the time-of-flight information for each event that triggered the system. Sufficient space was available to store ten complete events. When the storage buffer had been filled, the trigger mechanism and scaling equipment were gated off for approximately 15 msec while the contents of the buffer were written in a single record on magnetic tape. When writing had been completed, the storage buffer was cleared, and the whole system was reopened for storing more data.

D. Bias Settings and Relative Delays for the Neutron Counters

The efficiency for detecting neutrons with scintillation counters varies rapidly with the bias setting of the phototube. We obtained uniform bias settings for the counters in Array I by using a Na^{22} source, whose 1.3-MeV gamma rays provided adequate sensitivity, penetrated well into the scintillation material before being converted into electron-positron pairs, thereby eliminating surface effects. To set the bias of a tube, we adjusted the high voltage applied to the photomultiplier until the Na^{22} source produced between 4,000 and 8,000 net counts per second; this corresponds to approximately 20% of the γ rays passing from the source into the counter. The neutron-efficiency calibration (Sec. II-F) varified that this procedure set out tube biases uniformly at the required sensitivity.

Table II. Values of mean energy and mean $(p/\mu)^2$ for seven time-of-flight intervals.

Time bin	Flight time $t_n - t_\pi$ (nsec)	Bin width (nsec)	Mean energy and rms width (MeV)	Mean $(p/\mu)^2$ and rms width
τ_1	11.0 to 13.8	2.8	54±14	5.2±1.3
τ_2	13.8 to 16.9	3.1	38±12	3.6±1.1
τ_3	16.9 to 20.6	3.7	29±10	2.8±1.0
τ_4	20.6 to 24.9	4.3	23± 8	2.2±0.8
τ_5	24.9 to 29.4	4.5	18± 7	1.7±0.7
τ_6	29.4 to 35.8	6.4	13± 5	1.3±0.5
τ_7	35.8 to 42.8	7.0	10± 5	1.0±0.5

Measuring the energy of the final-state neutron by the time-of-flight method required setting the relative delays of all the tubes in Array I as nearly equal as possible. The narrowest of the seven timing intervals, listed in Table II, is 2.8 nsec; to validate measurements with this resolution the relative delays must be equalized to a small fraction of this width. This was done by a light-pulser technique. Each of the counters in Array I had, in the center of its face, a threaded socket into which a small light fixture could be screwed. The bulb in this fixture had a single filament and was filled with hydrogen gas;[14] when voltage was pulsed onto the filament, a low-level pulse of light was produced whose duration and intensity closely resembled the light produced by charged particles passing through a plastic scintillator. The beam counter S3, also equipped with a light-pulser socket, generated a trigger which activated the Chronotron; we timed each tube in Array I relative to S3 by plotting the number of counts received in Time Bin 1 (2.8 nsec wide) vs tube delay. The same light pulser and connecting lead were used on all tubes, and the intensity of the light fixture was adjusted until a standard voltage output was elicited from each tube. From the 84 delay curves thus patiently produced, the relative delays of all tubes in Array I were set equal to within 0.5 nsec.

This same light-pulser technique was used to time the signals arriving for storage in the data-storage system. In this instance, the full-trigger requirement for the system was simulated: as above, the light pulser in S3 supplied a pseudoscattering signature, T; a light pulser, delayed so that it would fire during the neutron flight-time interval, served as a pseudoneutron; the trigger system then sent gate drivers to the coincidence circuits at the entrance of the data-storage system. Each of these circuits had an auxiliary scaler output that could be counted. A third light pulser placed in any tube in either Array I or Array II (which also was equipped with light-pulser sockets) could be timed relative to the gate drivers that were supplied by the trigger system.

In this way we could set the relative delays of all the elements of Arrays I and II without using Bevatron running time.

The absolute delay settings were obtained by adding a 12.4-nsec delay to the neutron timing channel, Σ, so that those pions with $\beta \approx 1$, which were scattered from the incident beam, would appear at the time that neutrons with a 12.4 nsec flight time would ordinarily appear; the delay of the Chronotron trigger signal, T, was adjusted until these fast scattered particles fell in the center of Time Bin 1. When the 12.4-nsec delay cable was removed from Σ, the apparatus was correctly delayed to measure neutron time of flight.

Data were taken under four target and delay conditions: flask full and empty; delays normal and abnormal. The abnormal delay condition was achieved by adding 120 nsec to the neutron timing channel Σ, while keeping the delays of the triggering circuitry and Chronotron unaltered. Any slow particles detected under these conditions must have arrived at Array I 120 nsec earlier than usual and could not be causally related to the scattered meson that had triggered the system. The abnormal delay condition thus gave a measure of the purely accidental background in the neutron channels. In terms of these four conditions--full-normal, full-abnormal, empty-normal, and empty-abnormal--the net hydrogen-derived counting rate is given by

$$(\text{rate})_{\text{net}} = (\text{rate})_{\text{FN}} - (\text{rate})_{\text{EN}} - (\text{rate})_{\text{FA}} + (\text{rate})_{\text{EA}}. \qquad \text{(II-3)}$$

The standard deviation error, σ_{net}, is given by

$$(\sigma_{\text{net}})^2 = (\sigma_{\text{FN}})^2 + (\sigma_{\text{EN}})^2 + (\sigma_{\text{FA}})^2 + (\sigma_{\text{EA}})^2 \qquad \text{(II-4)}$$

from the familiar theorem of statistics[15] for combining independent, normally distributed quantities, and σ_{FN}, σ_{EN}, σ_{FA}, and σ_{EN} are the standard deviations associated with the full-normal, empty-normal, full-abnormal, and empty-abnormal rates, respectively.

E. Competing Channels

Interactions of π^- mesons in hydrogen give rise to many channels involving neutral pions:

$$\pi^- + p \rightarrow \pi^- + \pi^0 + p \qquad \text{(II-5a)}$$

$$\rightarrow \pi^0 + \pi^0 + n \qquad \text{(II-5b)}$$

$$\rightarrow \pi^- + \pi^+ + \pi^0 + n\,. \qquad \text{(II-5c)}$$

To avoid contamination from these channels, we placed a sheet of lead 0.25 in. thick over the inner faces of Arrays I and II. From Array I, including the 15 cm of plastic scintillator in the counters themselves, there were approximately 2 radiation lengths of material for pair production. Array II, whose counters are thin scintillators, was protected by about 1.6 radiation lengths. There was a probability of approx 95% that at least one of the two γ rays resulting from neutral pion decay would be converted into an electron-positron pair and thereby be detected. The rationale, imposed on us by the necessary thickness of Array I for neutron detection, was to render π^0 mesons detectable by our apparatus in order to eliminate contamination by processes (II-5).

The sheet of lead also filtered out proton final-state systems [e.g., (II-5a)]. Protons, because of their charge, lose energy first in their flight through liquid hydrogen, then in their passage through the lead sheet; to be detected in Array I they must be born in the target with more than 70 MeV of kinetic energy and traverse the 160-cm flight path with energies in excess of 60 MeV. This corresponds to flight times less than 11.5 nsec; i.e., at the front edge of Time Bin 1. This bracketing process keeps protons from triggering our apparatus and thus masquerading as low-energy neutrons.

F. Neutron-Efficiency Calibration

To validate the data taken with this apparatus at the Bevatron, it was necessary to have detailed knowledge of the efficiency with which Array I detected neutrons in the energy range 5 to 65 MeV; the neutron efficiency calibration was accomplished in a separate experiment performed at the Lawrence Radiation Laboratory 184-inch cyclotron. A description of this experiment and some of its results have been published separately,[16] so only a cursory discussion is given here, along with results not previously published that are specific to Array I and to the Chronotron employed in the time-of-flight measurement.

Deuterons, accelerated to 420 MeV in the 184-inch cyclotron, were stripped on an internal copper target; and the resultant beam of neutrons was extracted from the neutron port in the shielding wall of the cyclotron. Because of the internal motion of the deuteron, neutrons produced by stripping have a broad spectrum of energies; in this particular beam, the most probable energy was about 190 MeV, and the full-width-at-half-maximum energy was about 50 MeV. This beam, collimated by the neutron port into a rectangle 1.5 in. high and 0.5 in. wide, impinged on a liquid-hydrogen target. A differential range telescope composed of three plastic scintillation counters measured both the energy and angle of forward-scattered protons. The determination of both the energy and angle of these protons defined within narrow limits the energy of the incident neutron which had undergone an n-p scatter; in effect, we used only a narrow band of the broad energy spectrum of the incident beam. The differential range telescope thus defined a beam of recoil neutrons well determined in angle and in energy. Exact replicas of the counter elements used in Array I were placed in this beam of recoil neutrons. If C is the number of recoil protons detected in the differential range telescope and NC is the number of coincidences between the telescope and the neutron counter, then the neutron-detection efficiency is simply the ratio NC/C, if the neutron counter wholly covers the cone of scattered neutrons.

Additional and ultimately more useful data were obtained by removing the neutron counter to a distance of 160 cm from the hydrogen target and installing the Chronotron to time the neutrons. For neutrons of a given energy as defined by the proton differential range telescope, it was possible to measure the detection efficiency for each individual time bin. This technique determined the energy resolution for the time-of-flight measurement as well as the detection efficiency.

Measurements were made at a total of 13 neutron energies. The results are listed in Table III and plotted in Fig. 5 and Fig. 6a.

The efficiencies for the individual time bins (hereafter called resolution functions) deviate somewhat from a Gaussian form: they all are skewed, with high-efficiency tails extending toward higher neutron energies. A very plausible explanation of this comes from timing jitter introduced by poor photoelectron statistics. Detection of neutrons comes about largely through n-p scattering in the plastic scintillator; since the n-p differential scattering cross section in this energy range is roughly isotropic in the center-of-mass frame,[17] the proton energy spectrum in the laboratory frame is approximately flat. The high-energy portion of this spectrum deposits sufficient energy in the scintillator to produce high levels of light, which in turn educe large numbers of photoelectrons from the photocathode and generate output signals with very little timing jitter. As one passes toward lower-energy recoils, the situation degenerates: one finds low light levels, fewer photoelectrons, and timing jitter in the phototube output signals. For the lowest-energy part of the recoil spectrum, these difficulties are compounded by a saturation of the scintillator's ability to convert energy lost by the proton into light--the collision-loss rate, which for protons of a few MeV increases inversely as velocity, exceeds the amount of light energy the scintillator is capable of reradiating per unit length of path.[18] Regardless of incident neutron energy, the low-energy portion of the recoil spectrum gives rise to phototube outputs which, due to timing jitter, appear later than outputs from high-energy recoils. The Chronotron detects these in time bins

Table III. Neutron-detection efficiencies as a function of energy for the seven Chronotron flight-time intervals

Neutron energy (MeV)	Detection Efficiency							
	ϵ_1	ϵ_2	ϵ_3	ϵ_4	ϵ_5	ϵ_6	ϵ_7	$\epsilon_T = \sum_{i=1}^{7} \epsilon_i$
4.4	0	0	0	0	0	0	0.021 ±0.002	0.021 ±0.002
6.8	0	0	0	0	0	0.018 ±0.002	0.126 ±0.006	0.144 ±0.006
9.8	0	0	0	0.003 ±0.001	0.054 ±0.004	0.148 ±0.008	0.077 ±0.005	0.282 ±0.010
13.3	0	0	0.002 ±0.001	0.032 ±0.004	0.121 ±0.007	0.103 ±0.006	0.030 ±0.003	0.288 ±0.011
17.2	0	0.003 ±0.001	0.065 ±0.005	0.131 ±0.007	0.058 ±0.004	0.037 ±0.004	0.015 ±0.001	0.309 ±0.011
23.9	0.004 ±0.002	0.060 ±0.005	0.124 ±0.007	0.041 ±0.004	0.035 ±0.004	0.014 ±0.002	0.008 ±0.002	0.286 ±0.011
28.8	0.030 ±0.003	0.137 ±0.007	0.074 ±0.005	0.031 ±0.004	0.017 ±0.003	0.008 ±0.002	0.002 ±0.001	0.299 ±0.011
34.2	0.057 ±0.005	0.143 ±0.007	0.051 ±0.004	0.022 ±0.003	0.009 ±0.002	0.005 ±0.001	0.002 ±0.001	0.289 ±0.010
40.0	0.101 ±0.005	0.097 ±0.005	0.032 ±0.003	0.019 ±0.002	0.006 ±0.001	0.005 ±0.001	0	0.262 ±0.008
45.9	0.181 ±0.006	0.047 ±0.003	0.016 ±0.002	0.009 ±0.001	0.002 ±0.001	0.002 ±0.001	0	0.258 ±0.007
58.7	0.151 ±0.007	0.023 ±0.003	0.010 ±0.002	0.003 ±0.001	0	0	0	0.189 ±0.008
62.0	0.099 ±0.007	0.015 ±0.003	0.009 ±0.002	0.002 ±0.001	0	0	0	0.128 ±0.008
75.8	0.035 ±0.004	0.007 ±0.002	0.002 ±0.001	0	0	0	0	0.044 ±0.010

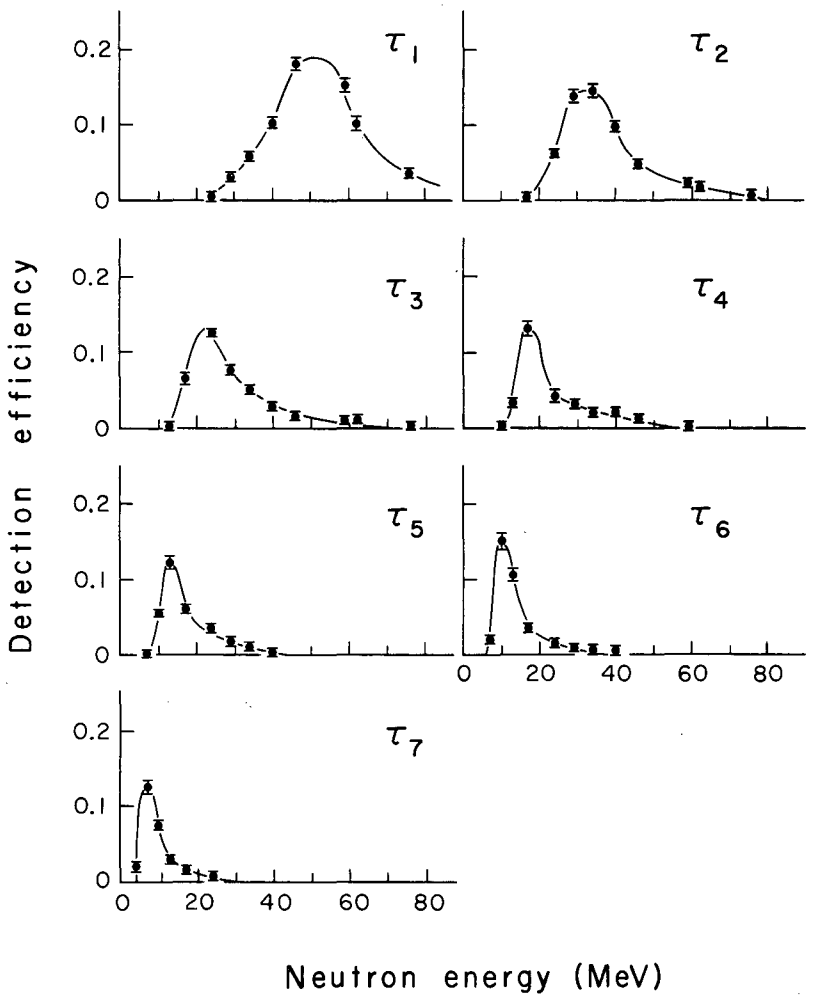

Fig. 5. Energy-resolution functions for the seven neutron flight-time intervals.

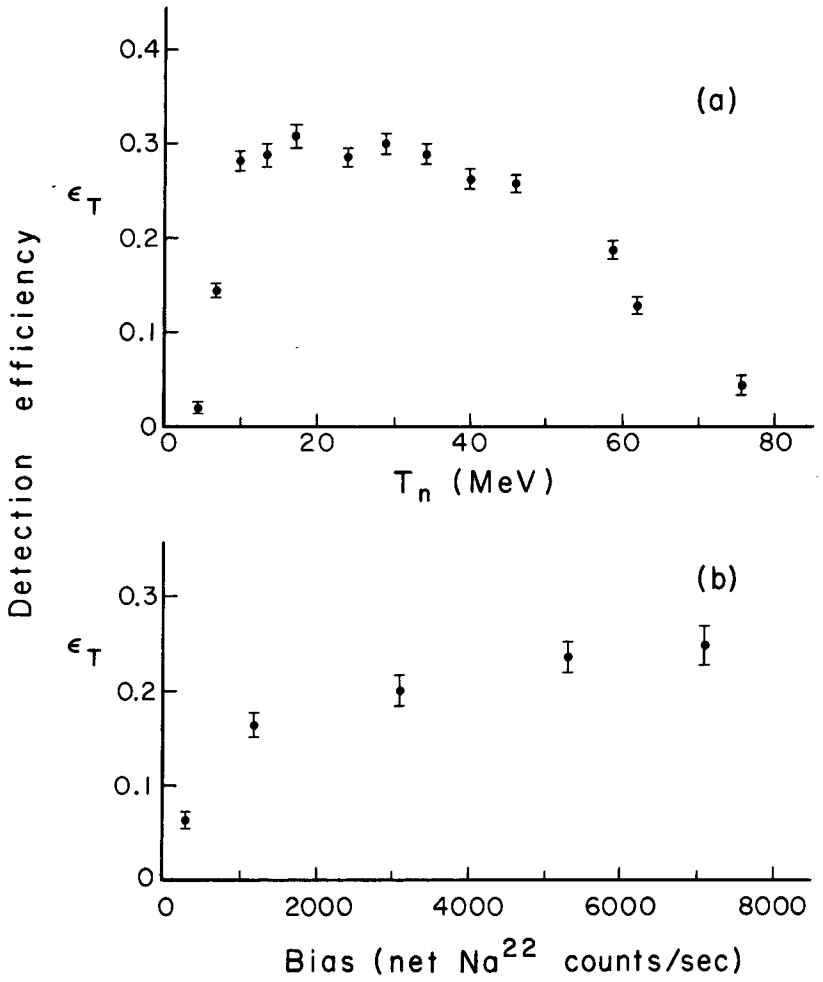

Fig. 6. (a) Total efficiency for detecting neutrons with counters in Array I. (b) Neutron-detection efficiency as a function of tube bias for 6.8-MeV neutrons.

which ordinarily detect lower-energy neutrons. Hence, there is a high-efficiency tail toward high neutron energies.

From the resolution functions one can calculate the mean neutron energies and the root-mean-square energy widths associated with each time bin. This material, as well as the flight-time information, has been summarized in Table I.

The curves drawn through the resolution-function data points are not fitted curves (attempts at fitting the data with a series of Hermite functions were unsuccessful; the high-energy tails require more terms than the data are capable of supporting) and are meant only to guide the eye and provide a continuous curve for calculations.

We checked our bias sensitivity by measuring the total efficiency for detection of 6.8-MeV neutrons as a function of bias setting (in net Na^{22} counts per second). The results are shown in Fig. 6b. Over the range of bias settings that we accepted, the efficiency for counting 6.8-MeV neutrons changes only a few percent.

Measurements were made with several different phototubes and several sizes of counters from Array I. Their efficiencies and timing responses seem to agree within the statistics of our measurements.

G. Proton-Proton Cross Sections at 310 MeV

We checked the ability of our apparatus to measure charged-particle cross sections by extracting a beam of 310-MeV protons with our beam channel and impinging them on the liquid hydrogen target. The detection apparatus, electronic system, and data storage and magnetic-tape equipment were used as described in Sec. II-C with the exception of the triggering system: delay was added to the Σ channel (neutron timing channel) so that scattered protons were in coincidence with the T signal of Eq. (II-1) and thus generated the necessary gate drivers to activate the data-storage system. In this way we measured the proton-proton total and differential cross sections. The total cross section

was 22.8±0.5 mb--in good agreement with other experiments. The differential cross section, plotted in Fig. 7, is seen to be isotropic in the center-of-mass frame with a value of about 3.5 mb/sr--also in good agreement with other experimental values.[19]

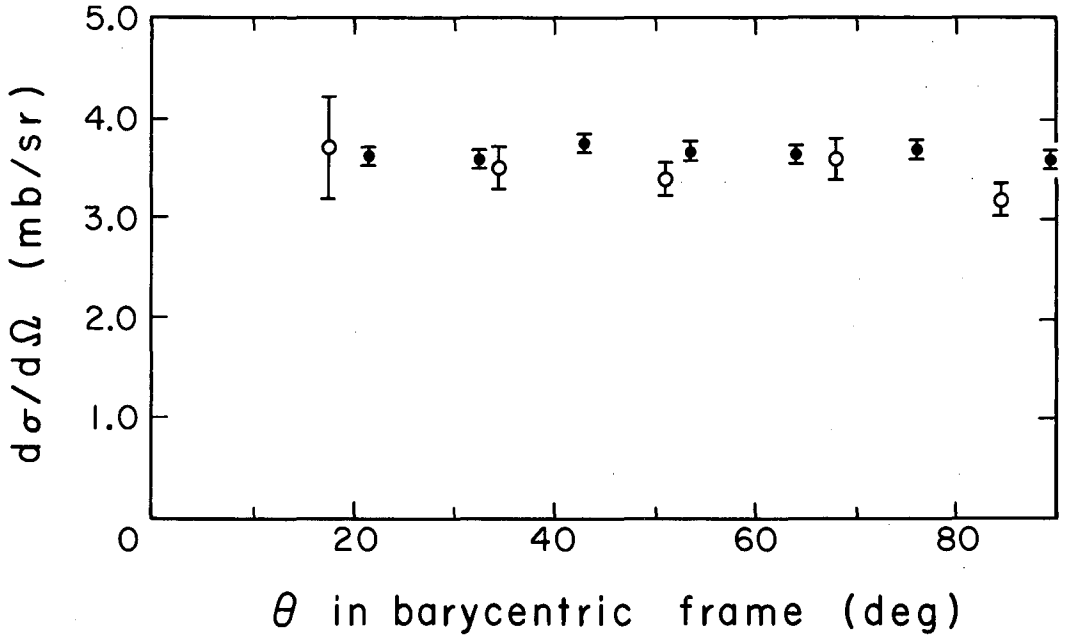

Fig. 7. Differential proton-proton cross section as a function of the scattering angle in the barycentric frame. Triangles refer to measurements made with Arrays I and II for 310-MeV incident protons. Solid dots refer to the measurements by Ypsilantis[19] at an incident energy of 315 MeV.

III. DATA HANDLING, REDUCTION, AND CORRECTIONS

A. The Analysis System (General Description)

As explained in Sec. II-C the primary data were recorded directly on magnetic tape. Two record lengths were employed.[20] The full core-storage buffer, containing complete information for ten scattering events of the type described in Section II, was transcribed onto tape as a single record containing 60 words. If the buffer was filled several times during a single Bevatron pulse, several 60-word records were written in tandem; at the end of each pulse, the contents of the buffer at that time (partially filled with data, the unfilled portion containing zeroes) were recorded as a 60-word record followed by a one-word identification record. The identification record contained the Bevatron Serial Number and the target and delay conditions for the data. During the 6-sec interval between pulses, the Bevatron Serial Number was advanced, and the core storage buffer was cleared in readiness for the next pulse. When a measurement under a given target and delay condition had been completed, the recording and scaler- monitoring equipment were turned off, and the tape was manually marked with an end of file. When a magnetic tape had been filled (typically about 3000 Bevatron pulses were recorded on a single tape), multiple ends of file were written on the tape to signify its completion.

The tapes were then analyzed by using the Lawrence Radiation Laboratory IBM 709 Data Processing System. The purpose of this analysis was twofold. Because of the complexity of the detecting apparatus (there were 102 individual scintillation counters in Arrays I and II), the analysis program prepared individual counting statistics on the number of particles detected by each element. Statistics were also compiled on the number and kind of particles (distinguished by fast or slow flight times) involved in each event. At the end of each file of the data tape, this information was printed out. While data were being taken at the Bevatron, at least one tape was processed each day to provide a running

check on the condition of the apparatus. From these statistical reports it was easy to locate malfunctioning counters.

The second function of the analysis program was (a) to screen the data for events with a two-pion, one-neutron signature, (b) to subject these events to a kinematical fit, and (c) to sort the data into a form useful for calculating the double distributions $d^2\sigma/d(w^2)d(p^2)$.

The analysis system produced two output tapes. The first was a binary-coded decimal ("Print") tape containing the summary of counter statistics and a sorted listing of all the two-pion, one-neutron events with partial results of the kinematical fitting. The second output tape (referred to as B-9 below) contained in binary form complete information for all two-pion, one-neutron events. A printed copy of the information on the first tape could be obtained by using standard IBM printing equipment; the second tape was not printable because of its condensed binary form, and served as a permanent record of the data.

The coding in the analysis program was a mixture of the FAP and FORTRAN coding languages: FORTRAN, which is a simple and condensed coding system,[21] was employed for arithmetic calculations and for binary-coded decimal output; FAP, the basic but more tedious language of the 709, was used for the complex logical structures of the program and for reading and writing binary tapes.

The analysis program read into core all the data recorded during one Bevatron pulse--i.e., 60-word records were read from the Bevatron data tape until an identification record was encountered. For each event, appropriate entries were made in the summary of counter statistics and the event was scanned for a two-pion, one-neutron signature. For events of this type a cursory check was made to see if transverse momentum balance were possible. An event was rejected whenever all three particles detected were contained in an azimuthal interval of less than 180 deg about the incident-beam direction. Events meeting this preliminary criterion were subjected to a detailed kinematical fit (see the following section, III-B.). Regardless of the outcome of fitting, complete

information concerning the event was transcribed on the B-9 output tape. Additionally, partial information was recorded on an intermediate tape. The information on this tape was sorted into 49 categories according to the time bin and polar angle of the neutron. The sorted data and the summary of counter statistics were recorded on the printable output tape.[9] This analysis cycle was repeated with each successive file of information on the data tape until a double end of file was encountered which signaled the completion of the data tape.

When all the data tapes at a given momentum had been processed, the B-9 output tapes were amalgamated in a packed and more condensed form onto a single binary tape. All subsequent analysis of the two-pion one-neutron events proceeded from this master tape.

B. Kinematical Fitting of the Data

Our experiment measures seven nontrivial parameters for each event: the polar angle of the neutron, θ_2; the neutron kinetic energy, T_2, determined from the time-of-flight information; the polar angle of each final-state pion, $\theta_{\pi 1}$ and $\theta_{\pi 2}$; the azimuthal angle (relative to the azimuthal position of the neutron) of each final-state pion, $\phi_{\pi 1}$ and $\phi_{\pi 2}$; and the momentum of the incident beam, q_{1L}, as determined by the beam-bending magnets. From the equations of four-momentum conservation, which are

$$\begin{aligned} q_{1L} &= p_2 \cos\theta_2 + p_{\pi 1} \cos\theta_{\pi 1} + p_{\pi 2} \cos\theta_{\pi 2} , \\ 0 &= p_2 \sin\theta_2 + p_{\pi 1} \sin\theta_{\pi 1} \cos\phi_{\pi 1} + p_{\pi 2} \sin\theta_{\pi 2} \cos\phi_{\pi 2} , \\ 0 &= p_{\pi 1} \sin\theta_{\pi 1} \sin\phi_{\pi 1} + p_{\pi 2} \sin\theta_{\pi 2} \sin\phi_{\pi 2} , \end{aligned} \tag{III-1}$$

and

$$\omega_{1L} + M_1 = \omega_2 + \omega_{\pi 1} + \omega_{\pi 2} ,$$

we observe that any five quantities completely determine the kinematics. The two redundant measurements must be consistent with the determining set of five within the resolutions imposed by the apparatus.

If the measured quantities were normally distributed, the χ^2 method of fitting and analysis could be applied to this problem.[22] However, measurements made by counting devices deviate considerably from the required normal distribution: detection of a particle by a scintillation counter delimits the position of the particle with certainty to the region occupied by the scintillation crystal; within this sensitive area the particle is everywhere equally probable. The angular measurements made in this experiment have very much this character; however, when we fold in the finite size of the liquid hydrogen target, we obtain in first approximation probability distributions which are trapezoidal rather than flat. As seen in the Sec. II-F, the energy-resolution functions for the neutron deviate from a pure Gaussian form.

The inapplicability of the χ^2 method was further shown during the design stages of the experiment in tests on trial samples of data. Using means and root-mean-square widths dictated by the trapezoidal probability distributions indicated above, we obtained the frequency distribution of χ^2 for a trial sample of kinematically valid events. This distribution peaked sharply around $\chi^2 = 0$, with a long, flat tail toward higher values of χ^2; there was a marked deviation from the theoretical χ^2 distribution with one degree of freedom.

These considerations and difficulties evolved into the following philosophy: if an exact kinematical solution to the two-pion one-neutron hypothesis could be found within the resolutions of measurement, then that event must be accepted. This approach avoids interpreting a statistical fitting parameter and yet cannot discriminate against actual two-pion one-neutron events.

The method was implemented by a gradient-search technique conducted within the domains of the measured variables as delimited by the resolutions of the apparatus. The set of variables θ_2, T_2, q_{1L}, $\theta_{\pi 1}$, and $\phi_{\pi 1}$ (hereafter called defining set) were chosen as the five variables determining the kinematics. From the system of Eqs. (III-1), we may find $\theta_{\pi 2}$ and $\phi_{\pi 2}$ in terms of the defining set

$$\theta_{\pi 2} = \Theta\,(\theta_2,\ T_2,\ q_{1L},\ \theta_{\pi 1},\ \phi_{\pi 1})\ ,$$

and

$$\phi_{\pi 2} = \Phi\,(\theta_2,\ T_2,\ q_{1L},\ \theta_{\pi 1},\ \phi_{\pi 1})\ , \qquad \text{(III-2)}$$

where Θ and Φ, because of their algebraic complexity, are listed separately in Appendix A.

The mathematical statement of this approach requires two parameters, G_1 and G_2, defined by

$$G_1 = \left| \frac{\theta_{\pi 2} - \theta_{\pi 2}{}^0}{\Delta\theta_{\pi 2}} \right| ,$$

and

$$G_2 = \left| \frac{\phi_{\pi 2} - \phi_{\pi 2}{}^0}{\Delta\phi_{\pi 2}} \right| . \qquad \text{(III-3)}$$

The variables $\theta_{\pi 2}$ and $\phi_{\pi 2}$ are calculated from (III-2); $\theta_{\pi 2}{}^0$ is the centroid in polar angle of the counter in which the pion was detected; similarly, $\phi_{\pi 2}0$ is the azimuthal centroid of the counter; $\Delta\theta_{\pi 2}$ and $\Delta\phi_{\pi 2}$ are the half-widths of the polar and azimuthal intervals, respectively, subtended by the counter (including effects of finite target size). Table IV summarizes $\theta_{\pi 2}{}^0$, $\phi_{\pi 2}{}^0$, $\Delta\theta_{\pi 2}$, and $\Delta\phi_{\pi 2}$ for Arrays I and II.

An exact kinematical solution to the two-pion one-neutron hypothesis had been found whenever G_1 and G_2 were simultaneously less than one and the defining set of variables was within the measured resolutions. Let us call this condition the "fitting criterion."

To guide the search of the defining set of variables toward achievement of the fitting criterion, the negative gradients of G_1 and G_2 with respect to the defining set were calculated:

$$\vec{g}_1 = -\ \mathrm{grad}(G_1)\ ,$$

and

$$\vec{g}_2 = -\ \mathrm{grad}(G_2), \qquad \text{(III-4)}$$

when $\vec{g}_1$ and $\vec{g}_2$ are five-dimensional vectors in the hyperspace of

Table IV. Angular intervals subtended by counters in Arrays I and II. With a point target, all counters subtended 30 deg in azimuthal angle. The effect of finite target size gives the counters a physical size $30^{\circ} + 2\delta\phi$.

Array	Theta zone	Point-target limits		Physical limits		
		θ_{min}	θ_{max}	θ_{min}	θ_{max}	$\delta\phi$
I	1	4	12	2.2	14.1	13.8
	2	12	20	9.9	23.3	4.7
	3	20	28	17.7	30.5	2.8
	4	28	36	25.5	38.7	2.0
	5	36	44	33.4	46.8	1.6
	6	44	52	41.3	54.9	1.4
	7	52	60	49.2	62.9	1.2
II	8	54.5	70	57.8	81.4	5.3
	9	70	90	58.1	102.2	5.3
	10	90	110.5	77.8	122.8	5.3
	11	110.5	147.5	98.6	155.1	5.3

the defining set of variables. The scalar product $(\vec{g}_1 \cdot \vec{g}_2)$ determined the path of the search as follows:

(a) if $(\vec{g}_1 \cdot \vec{g}_2) < 0$, the search moved along $\vec{g}_1 + \vec{g}_2$;

(b) if $(\vec{g}_1 \cdot \vec{g}_2) \leq 0$, the path of the search depended on the relative magnitudes of G_1 and G_2. For example, if $G_1 > G_2$, the search proceeded along the direction $\vec{v}$:

$$\vec{v} = \vec{g}_1 - (\vec{g}_1 \cdot \vec{g}_2) \frac{\vec{g}_2}{(g_2^2)} ,$$

i.e., along a path perpendicular to $\vec{g}_2$. Similarly if $G_2 > G_1$, a path perpendicular to $\vec{g}_1$ was followed. A path so chosen either decreases both G_1 and G_2 (choice a) or decreases the larger of G_1 and G_2 while holding the smaller fixed (choice b).

With the path of the search thus specified, the step size along this path was chosen to reduce the larger of G_1 and G_2 to a value of 1, as required by the fitting criterion. If such a step brought any of the determining variables outside their specified resolution, that variable was not allowed to step the full distance but was held at the extremity permitted by its resolution.

An event was rejected if the fitting criterion was not fulfilled after twelve such steps or if a stalemate situation was encountered--i.e., if all the defining variables were pinioned at the extremities of resolution and if the gradients required a path which crossed the boundaries. Two empirical tests showed that twelve steps were sufficient: a sample of 600 kinematically valid events was all easily found in 12 steps; we analyzed a Bevatron data tape first using 12 steps, then using 20 steps-- the net number of kinematical fits changed by less than 1% between the two conditions of analysis.

C. Rejection Efficiency of Kinematical Fitting

A method of fitting that we explored during the design stages of the experiment provided an estimate of the rejection efficiency of the fitting procedure. We attempted to generate a "directory" of all the two-pion one-neutron signatures which, following the philosophy of Sec. III-B, contained within the resolutions of measurement an exact solution to the two-pion one-neutron hypothesis. Exact solutions for this hypothesis were generated by a computer program and translated into a set of numbers appropriate to the neutron flight time and to the counters of Arrays I and II; these sets of numbers were then arranged in tabular form. We continued to generate solutions until the table approached saturation. Our analysis of data tapes, had this scheme been used, would then have been reduced to a scan of this table for an entry corresponding to the event under analysis; if an entry were present, the event would be accepted, otherwise it would be rejected.

Generating such tables was time-consuming and lacked the versatility required by our experiment; each incident momentum required a separate table, and any changes in the apparatus during the experiment would have necessitated an entirely new directory. As a result, this method of analysis was abandoned after only one partial directory had been compiled: this was a directory of events for an incident-pion momentum of 1.75 BeV/c in which both final-state pions were detected in Array I. The 84 elements of Array I provide

$$\frac{(84)\,(83)\,(82)}{(12)} = 47{,}642$$

possible ways of distributing three particles (the factor of 12 arises from azimuthal symmetry of the events about the incident beam direction). Additionally, there are seven flight-time intervals that the neutron may occupy. The partial directory therefore contains roughly 300,000 possible entries. Of these, we found approximately 20,000 which contained exact solutions to the two-pion one-neutron hypothesis. The resultant rejection efficiency for a background of purely random two-pion one-neutron events is therefore 15 to 1.

D. Reduction of the Data to Cross Sections

To use the Chew-Low method of analysis outlined in Sec. I, the data must be reduced to the double distributions $d^2\sigma/d(p^2)d(w^2)$. The variables w^2 and p^2 are not directly observed laboratory system quantities but are related uniquely through Eq. (I-2) to the neutron kinetic energy, T_2, and $\cos\theta_2$. Therefore, the first step in the reduction was to sort the two-pion one-neutron events that satisfied the fitting criterion according to the neutron time bin and θ interval. Such a classification led to 49 categories (seven time bins and seven θ intervals in Array I) which we will denote in a matrix notation by the subscripts i and j. Let i represent the time bin and j the θ interval of the neutron.

This sorting process was carried out by an IBM 709 computer program which scanned the master data tape described above. A separate matrix of events was obtained for each target and delay condition. Each matrix was then normalized to the incident flux of π mesons and the number of protons per cm^2 in the liquid hydrogen target; the result was expressed in μb. This resulted in four matrices, one for each target and delay condition, whose elements we denote by r^{FN}_{ij}, r^{EN}_{ij}, r^{FA}_{ij}, and r^{EA}_{ij}. The superscripts refer to the target and delay conditions discussed in Section II; the subscripts refer to the 49 categories defined above. Each element signifies the counting rate in μb associated with those events whose neutron fell in the category ij.

In parallel with these matrices, four others were prepared--σ^{FN}_{ij}, σ^{EN}_{ij}, σ^{FA}_{ij}, and σ^{EA}_{ij} --which summarized the standard deviation errors due to counting statistics associated with each element of the matrices above.

The net counting rate R_{ij} in μb for the category ij was obtained by using Eq. (II-3):

$$R_{ij} = r^{FN}_{ij} - r^{EN}_{ij} - r^{FA}_{ij} + r^{EA}_{ij}.$$

The corresponding standard deviation errors ΔR_{ij} were calculated by using Eq. (II-4):

$$(\Delta R_{ij})^2 = (\sigma^{FN}_{ij})^2 + (\sigma^{EN}_{ij})^2 + (\sigma^{FA}_{ij})^2 + (\sigma^{EA}_{ij})^2 .$$

The next step in the reduction was to study the area $[2\pi\, dT_2\, d(\cos\theta_2)]_{ij}$ associated with each category ij and the transformation of that area into w^2-p^2 space. Let us denote the neutron-energy resolution function for the jth time bin (measurement of which was discussed in Sec. II) by $\epsilon_j(T_2)$. The portion of an infinitesimal interval dT_2 in a neighborhood about T_2 observed in the jth time bin is $\epsilon_j(T_2)dT_2$. Let us now define an angular resolution function $\eta_i(\cos\theta_2)$:

$$\eta_i(\cos\theta_2) = \begin{cases} 1, & \text{if } \theta_2 \text{ is within } \theta \text{ interval i;} \\ 0, & \text{if } \theta_2 \text{ is outside } \theta \text{ interval i.} \end{cases}$$

The portion of $[2\pi d(\cos\theta_2)]$ observed in θ interval i is formally given by $(2\pi\, \eta_i(\cos\theta_2)\, d(\cos\theta_2))$. By combining these results we obtain the amount of the area element $[2\pi\, dT_2\, d(\cos\theta_2)]$ that is associated with category ij:

$$[2\pi dT_2 d(\cos\theta_2)]_{ij} = \epsilon_j(T_2)\,\eta_i(\cos\theta_2)\, 2\pi\, dT_2\, d(\cos\theta_2). \qquad \text{(III-5)}$$

A well-known theorem[23] relates $dT_2 d(\cos\theta_2)$ to $d(w^2)d(p^2)$ by the Jacobian of the transformation given in Eq. (I-2). Thus,

$$d(w^2)d(p^2) = \left\| \begin{matrix} \frac{\partial(p^2)}{\partial T_2} & \frac{\partial(p^2)}{\partial(\cos\theta_2)} \\ \frac{\partial(w^2)}{\partial T_2} & \frac{\partial(w^2)}{\partial(\cos\theta_2)} \end{matrix} \right\| 2\pi\, dT_2 d(\cos\theta_2)$$

$$= 4q_1 L p_2 M_2\, 2\pi\, dT_2 d(\cos\theta_2) . \qquad \text{(III-6)}$$

Applying this to Eq. (III-5) and integrating over T_2 and $\cos\theta_2$ yield the area in w^2-p^2 space associated with category ij:

$$A_{ij} = 4q_{1L}M_2 \int_0^{\infty} \epsilon_j(T_2)p_2 d(T_2) \int_0^{\pi} \eta_i(\cos\theta_2)\, 2\pi\, d(\cos\theta_2). \quad \text{(III-6)}$$

Using A_{ij} as a normalizing factor, we may construct $P_{ij}(w^2, p^2)$, the distribution function in w^2-p^2 space:

$$P_{ij}(w^2, p^2)d(w^2)d(p^2) = \frac{\epsilon_j(T_2)\,\eta_i(\cos\theta_2)}{A_{ij}}\, 4q_{1L}p_2M_2 2\pi dT_2 d(\cos\theta_2).$$

This definition ensures the normalization

$$\int_{\Gamma} P_{ij}(w^2, p^2)d(p^2)d(w^2) =$$

$$\frac{4q_{1L}M_2}{A_{ij}} \int_0^{\infty} \epsilon_j(T_2)p_2 d(T_2) \int_0^{\pi} \eta_i(\cos\theta_2)\, 2\pi\, d(\cos\theta_2) \equiv 1,$$

where Γ is the region in w^2-p^2 space which is kinematically allowed. The mean values of p^2 and w^2 for category ij are then given by

$$\left\langle (w^2)_{ij} \right\rangle = \int_{\Gamma} P_{ij}(w^2, p^2)w^2 d(w^2)d(p^2)$$

$$= \frac{4q_{1L}M_2}{A_{ij}} \int_0^{\infty} \epsilon_j(T_2)p_2 d(T_2) \int_0^{\pi} w^2(T_2, \cos\theta_2)\, \eta_i(\cos\theta_2) \times 2\pi d(\cos\theta_2)$$

$$\left\langle (p^2)_{ij} \right\rangle = \int_{\Gamma} P_{ij}(w^2, p^2)\, p^2 d(w^2)d(p^2)$$

$$= \frac{4q_{1L}M_2}{A_{ij}} \int_0^{\infty} \epsilon_j(T_2)p_2 d(T_2)p^2(T_2) \int_0^{\pi} \eta_i(\cos\theta_2)\, 2\pi d(\cos\theta_2). \quad \text{(III-7)}$$

We complete the reduction by calculating the average value of the desired double distribution over category ij:

$$(d^2\sigma/d(w^2)d(p^2)\,)_{ij} = R_{ij}/A_{ij}\,. \qquad \text{(III-8)}$$

The standard deviation error is given by

$$\Sigma_{ij} = \Delta R_{ij}/A_{ij}\,. \qquad \text{(III-9)}$$

The values of p^2 and w^2 appropriate to the measure are $\langle (p^2)_{ij} \rangle$ and $\langle (w^2)_{ij} \rangle$ as defined above.

E. Scattering Corrections Applied to the Data

Two scattering processes inherent in our apparatus introduced sizable distortions into the data.

The first process involves scattering of final-state pions in the thick scintillators of Array I. A high-energy pion, scattering inelastically in one of these 15-cm-thick scintillators, could pass into an adjacent counter and appear in our analysis scheme as a three-pion one-neutron signature. Correction for such processes is discussed in Sec. 1 following.

The second process deals with rescattering of final-state neutrons as they emerge from the liquid hydrogen target. At 10 MeV the neutron-proton scattering cross section is approximately 1 barn, and it rises inversely with energy below 10 MeV. Such large cross sections make neutron rescattering important for the low-energy part of the neutron spectrum. This correction is discussed in Sec. 2.

Because the scattering processes and detection apparatus were complicated, these corrections were approached by the Monte Carlo method. A discussion of this method and the details of its present application are given separately in Appendix B.

1. Pion Scattering Correction

A pion passing into an element of Array I sees first 0.6 cm of lead, then 15 cm of plastic scintillator (CH) which is composed of an

equal number of carbon and hydrogen atoms. We are interested in calculating the probability that a pion scatters into an adjacent element. To do this precisely we must know the scattering cross sections, multiplicities, and angular distributions for pion-carbon and pion-lead scattering as a function of energy. A survey of the literature[24-26] indicates that certain simplifying assumptions may be made, indeed must be made, since complete information is not available:

(a) The first assumption is to neglect elastic scattering. The angular distributions for elastic processes are diffraction-peaked in the forward direction and seldom lead to scattering angles large enough to deflect pions into an adjacent counter.

(b) The absorption cross section for π^- on carbon is approximately flat at 250 mb from 400 MeV to above 1 BeV;[24] this leads us to assume no energy dependence for the scattering cross sections.

(c) Average cross sections for carbon, hydrogen, and lead indicate that 80% of the scattering arises from the carbon in the plastic scintillator. This information is listed in Table Va. We choose to neglect the scattering from the other constituents in comparison to carbon.

(d) Measurement of angular distributions at 915 MeV for π^- on carbon indicate approximate isotropy for inelastic processes. We may either assume isotropy or adopt these angular distributions at all energies.

A Monte Carlo calculation was performed using the above information; the paths of 4000 pions were followed as they passed through a typical counter in each θ ring of Array I. Scattering events were generated according to four hypotheses:

I. A geometric scattering cross section (330 mb); isotropic angular distributions; a multiplicity of one.

II. A scattering cross section of 250 mb; the measured π^--C angular distribution at 915 MeV; a multiplicity of one.

III. A scattering cross section of 250 mb; the measured π^--C angular distributions at 915 MeV; the multiplicities found in π-p collisions.[26]

Table Va. Scattering from the three constituents of counters in Array I.

Material	σ_{absorp} average (mb)	Amount of material	Scattering (%)	Fraction of total scattering
C	250	14.8 g/cm^2 (1.23 moles)	17	0.81
H	20	1.2 g/cm^2 (1.23 moles)	1	0.05
Pb	1700	7.2 g/cm^2 (0.03 mole)	3	0.14

IV. A scattering cross section of 250 mb; the angular distributions and multiplicities found in scattering of 915-MeV π^- from carbon.

The fraction of paths that passed into adjacent counters is summarized in Table Vb for each hypothesis. The errors listed are due to the Monte Carlo statistics amassed. The results are insensitive to the hypotheses assumed, and hypothesis III was selected as a representative average.

The results of this calculation were applied to the data by weighting each event by an appropriate correction factor. This weighting process was incorporated into the computer program that calculated the rates r^{FN}_{ij}, r^{EN}_{ij}, r^{FA}_{ij}, r^{EA}_{ij}, and R_{ij} described in the previous section. The correction factor depended on the pions detected in the event: if both pions were detected in Array I, the appropriate correction was

$$\frac{1}{(1-b(m))} \cdot \frac{1}{(1-b(n))} ,$$

where m and n are the θ intervals associated with each pion and b(i) is the scattering probability (as calculated above) for a pion in θ ring i; similarly, if one pion were detected in Array I and the other in Array II, the correction factor was taken as

$$\frac{1}{[1-b(m)]} .$$

In this fashion we obtained the net counting rate R'_{ij} corrected for pion scattering.

To check the validity of the scattering correction, we examined our raw data tapes for events in which the final-state pions appear to have scattered from one element to another. A computer program was written which scanned the original Bevatron data tapes for events with either a three-pion one-neutron or a four-pion one-neutron signature. Whenever the pions fell in adjacent counters and appeared as a possible event in which one or both pions had undergone scattering, the event was subjected to a kinematical fit. Analogous to the R_{ij} of the previous

Table Vb. Scattering of pions into adjacent elements for counters in Array I.

	Percent scattering into adjacent elements for θ ring						
Hypothesis	1	2	3	4	5	6	7
I	13.2 ±1.1	10.8 ±1.0	11.6 ±1.1	10.1 ±1.0	11.6 ±1.1	10.0 ±1.0	9.9 ±1.0
II	11.7 ±0.5	11.4 ±0.5	12.1 ±0.6	11.9 ±0.5	11.1 ±0.5	11.2 ±0.5	10.5 ±0.5
III	13.8 ±0.6	12.9 ±0.6	13.2 ±0.6	12.9 ±0.6	12.8 ±0.6	12.1 ±0.6	11.3 ±0.5
IV	14.3 ±0.6	14.4 ±0.6	14.3 ±0.6	14.6 ±0.6	14.2 ±0.6	13.9 ±0.6	12.6 ±0.6

section, let us define the net rate in category ij of "adjacent" events that meet the fitting criterion to be D_{ij}. For purposes of comparison we construct the following "raw" cross sections:

$$\sigma_0^m = \sum_{i=1}^{7} \sum_{j=1}^{7} (R_{ij}) ,$$

$$\sigma_1^m = \sum_{i=1}^{7} \sum_{j=1}^{7} (R_{ij} + D_{ij}) , \qquad \text{(III-10)}$$

and

$$\sigma_1^c = \sum_{i=1}^{7} \sum_{j=1}^{7} (R'_{ij}) ,$$

where σ_0^m is the uncorrected cross section, σ_1^m is the cross section corrected by a rescanning of the Bevatron data tapes for "adjacent" events, and σ_1^c is the cross section corrected in accordance with the Monte Carlo calculation. For the data at an incident momentum of 1.75 BeV/c, we find the ratios

$$\sigma_1^m/\sigma_0^m = 1.19 \pm 0.03,$$

and

$$\sigma_1^c/\sigma_0^m = 1.24 \pm 0.01.$$

The agreement is reasonably good. Indeed, the first ratio should be smaller than the second, since σ_1^m does not include events in which the scattered pion passes through more than one adjacent counter.

2. Neutron Rescattering Correction

A neutron that scatters in its passage out of the hydrogen target distorts our measurements in two ways. The scattering process alters the energy and direction of the neutron; an event which correctly belongs in category ij may be erroneously detected in category $i'j'$. Also, scattering destroys the kinematical consistency of the event; for large-angle rescattering the neutron may miss Array I completely or have its energy and angle sufficiently changed to fail the fitting criterion.

To solve this twofold problem a second Monte Carlo calculation was performed. A computer program was written which, given the four-momenta of the final-state particles, performed the following operations:

(a) an interaction center was selected in the hydrogen target weighted in accordance with the spatial distribution of the incident beam (a full-width at one-half maximum of 5 cm);

(b) the path of the neutron through the hydrogen target was followed in steps one-tenth the radius of the target, scattering events being generated in accordance with the n-p total cross section; if scattering occurred, the new path and energy of the neutron were calculated by use of n-p differential cross-section data;

(c) when the neutron emerged from the hydrogen target, the spatial coordinates of the pions and neutron were translated into corresponding counter numbers in Arrays I and II and the energy of the neutron was related to an appropriate time bin in accordance with the measured resolution functions (see Sec. II-F);

(d) if the neutron rescattered, a kinematical fit was attempted;

(e) for each of the 49 categories a log was kept of the various classes into which the event could fall:

(1) no rescattering,

(2) rescattering from category ij to category $i'j'$,

(3) rescattering out of the angular region covered by Array I or out of the interval of flight times detected by the Chronotron, and

(4) rescattering with sufficient distortion to fail the fitting criterion.

The events used as a sample in the calculation were those on the "master" tape, taken with full-normal target and delay conditions, which had passed the fitting criterion. We felt those events provided the best available approximation to the process as it occurred naturally.

We can summarize the results of this calculation with a set of coefficients $C^{ij}_{i'j'}$ which represent the probability that a neutron will rescatter from an initial category ij to a final category $i'j'$. By introducing the indices

$$n = 7(i - 1) + j \,, \qquad \text{and} \qquad m = 7(i' - 1) + j' \,, \tag{III-11}$$

the coefficients may be arranged in matrix form:

$$A_{mn} = C^{ij}_{i'j'} \,. \tag{III-12}$$

Similarly, the measured net rates R_{ij} of Sec. III-D form a column vector x_m; we also introduce the vector y_n to represent the true counting rates (corrected for rescattering). Apparently these quantities are related by the matrix equation

$$x_m = \sum_{n=1}^{49} A_{mn} y_n \,. \tag{III-13}$$

From the theory of linear equations,[27] we may obtain the corrected column y_n in terms of the inverse matrix $(A^{-1})_{mn}$ and x_m:

$$y_n = \sum_{m=1}^{49} (A^{-1})_{nm} x_m \,. \tag{III-14}$$

The standard-deviation errors associated with the corrected column y_n must reflect both the uncertainty in the initial column x_m [which we denote by $(\Delta x)_m$] and the statistical uncertainty in the Monte Carlo coefficients A_{mn} [which we denote by $(\Delta A)_{mn}$]. An expression is derived in Appendix B for the uncertainty in the y_n [which we symbolize as $(\Delta y)_n$] as a function of $(\Delta x)_m$, $(\Delta A)_{mn}$, y_n, and $(A^{-1})_{mn}$:

$$(\Delta y)_m^2 = \sum_{j=1}^{49} \left[(A^{-1})_{mj} (\Delta x)_j \right]^2 + \sum_{i=1}^{49} \sum_{j=1}^{49} \left[(A^{-1})_{mi} y_j (\Delta A)_{ij} \right]^2 \,. \tag{III-15}$$

Sufficient Monte Carlo statistics were amassed so that the percentage error $(\Delta y)_k/y_k$ was increased 10% at most over $(\Delta x)_k/x_k$ for any given k.

The magnitude of the rescattering correction varied between 2 and 10%, an amount somewhat smaller than the experimental uncertainty $(\Delta x)_k/x_k$ resulting from counting statistics. The correction is smaller than one might at first imagine, since 10-MeV neutrons traversing 5 cm of liquid hydrogen (half the target length) undergo approx 20% scattering. The smaller correction is a result of the cross-feeding of neutrons from one category to another. Rescattering tends to increase the number of low-energy neutrons; the effect is cumulative. Although neutrons in categories 7j suffer 20% scattering, they are compensated by rescattering from all higher-energy categories. These effects tend to cancel and the correction to the data is small.

F. Backgrounds

As explained above, the net counting rate in any category is obtained by using Eq. (II-3) to combine the full-normal, empty-normal, full-abnormal, and empty-abnormal rates. The validity of the subtraction process depends on the magnitude and nature of the backgrounds. Table VI lists the raw counting rate for each target and delay condition and gives indication of the relative sizes of the backgrounds. The rates shown are not corrected for neutron counting efficiency; they constitute raw total cross sections (in μb) over the region of w^2 and p^2 covered by our apparatus.

The backgrounds are not unduly large: at 1.75 BeV/c the respective ratios of the four effects are 1:0.23:0.03:0.02; at 1.25 BeV/c they are 1:0.31:0.05:0.02.

The source of the target-empty background is apparent: scattering processes occurred in the flask and thin windows of the hydrogen target as well as in counter S3 located directly before the target.

The source of the abnormal-delay backgrounds is less apparent. Such events involved detection of accidental neutrons--phototube pulses

Table VI. Raw cross sections for the various target and delay conditions.

Incident beam momentum (BeV/c)	Raw cross section (in μb) for the target and delay condition				Net cross section (μb)
	Full normal	Empty normal	Full abnormal	Empty abnormal	
1.25	293 ± 3.9	90 ±3.2	15 ±1.5	6 ±1.1	194 ± 5.3
1.75	309 ± 2.5	72 ±2.0	10 ±1.0	5 ±1.0	232 ± 3.6

not correlated with the incident particle that triggered the apparatus. These may be either beam-derived or related to noise in the photomultiplier tubes. In the first case one would expect the counting rate to depend on the beam intensity, in the second case to be independent of beam level. Data taken at different beam levels indicate the second case. Indeed, the abnormal delay rates are consistent with the noise level of the phototubes in Array I.

We therefore conclude that the background rates are sufficiently small and stable (independent of beam intensity) to justify the subtraction process.

G. Contaminations

We rely on kinematical fitting to protect the data against contamination from many particle-production processes that may simulate a two-pion one-neutron signature. As stated above, the fitting procedure has an estimated rejection efficiency of 15 to 1. Depending on the ratio of the true and simulated two-pion one-neutron rates, the events that meet the fitting criterion contain some contamination.

If r is the kinematical rejection efficiency and f is the fraction of the total two-pion one-neutron signatures that fit kinematics, one can easily calculate the percentage contamination to be

$$\frac{r}{1-r} \cdot \frac{1-f}{f} .$$

At 1.75 BeV/c we find $f = 0.45$, indicating 9% contamination. At 1.25 BeV/c we find $f = 0.32$, indicating 15% contamination.

The distribution of those events which fail the fitting criterion is approximately uniform in the variable w^2 and increases slowly as we move toward lower values of p^2. One would expect the contamination to be similarly distributed; and therefore the contamination might slowly increase as we pass to lower p^2.

The statistical accuracy of the data after division into the 49 categories is seldom better than 10% at 1.75 BeV/c or 15% at 1.25 BeV/c. The contamination, although it is not negligible, contributes less than the fluctuations intrinsic in the counting statistics.

H. The Double Distributions

The double distributions $d^2\sigma/d(p^2)d(w^2)$, corrected as described above, are presented in Tables VII and VIII. Figures 8 and 9 depict the data as a function of w^2 and p^2. The solid curves represent a least-squares fit to the data in the variable w^2 (see Sec. IV-A).

The errors quoted include both counting statistics and Monte Carlo statistics from the corrections applied to the data.

Table VII. Double distributions $d^2\sigma/d(p^2)d(w^2)$ in μb and mean w values in MeV at 1.25 BeV/c incident momentum.

Time bin		θ zone						
		1	2	3	4	5	6	7
τ_1	$\langle w \rangle$ =	755	740	715	675	625	560	475
	$\frac{d^2\sigma}{dp^2dw^2}$	16.0 ±2.5	14.5 ±1.6	12.5 ±1.4	6.3 ±0.8	4.4 ±0.7	4.9 ±0.7	2.6 ±0.4
τ_2	$\langle w \rangle$ =	710	695	675	645	600	540	470
	$\frac{d^2\sigma}{dp^2dw^2}$	23.5 ±4.4	26.0 ±3.0	18.5 ±2.4	16.2 ±1.9	14.2 ±1.6	6.4 ±1.1	5.1 ±1.0
τ_3	$\langle w \rangle$ =	680	665	645	615	580	525	460
	$\frac{d^2\sigma}{dp^2dw^2}$	26.6 ±6.0	23.1 ±4.0	16.7 ±3.2	14.0 ±2.1	8.5 ±1.9	6.1 ±1.5	5.5 ±1.3
τ_4	$\langle w \rangle$ =	655	640	620	595	555	510	450
	$\frac{d^2\sigma}{dp^2dw^2}$	41.3 ±7.0	20.2 ±4.6	25.0 ±3.9	17.5 ±2.6	14.4 ±2.1	7.0 ±1.8	4.5 ±1.7
τ_5	$\langle w \rangle$ =	620	605	590	565	530	490	435
	$\frac{d^2\sigma}{dp^2dw^2}$	21.0 ±8.6	24.4 ±5.4	21.2 ±4.3	13.7 ±3.1	13.4 ±2.6	11.9 ±2.1	6.4 ±1.7
τ_6	$\langle w \rangle$ =	585	575	560	535	505	465	420
	$\frac{d^2\sigma}{dp^2dw^2}$	14.6 ±12.5	28.1 ±6.1	22.8 ±5.7	24.6 ±4.3	15.4 ±3.4	11.1 ±3.0	3.1 ±2.7
τ_7	$\langle w \rangle$ =	550	540	525	505	475	445	400
	$\frac{d^2\sigma}{dp^2dw^2}$	33.2 ±15.4	12.2 ±8.9	18.5 ±7.2	15.6 ±5.5	14.3 ±4.6	11.0 ±3.5	4.4 ±3.7

Table VIII. Double distributions $d^2\sigma/d(p^2)d(w^2)$ in μb and mean w values in MeV at 1.75 BeV/c incident momentum.

Time bin		θ zone						
		1	2	3	4	5	6	7
τ_1	$\langle w \rangle =$	910	890	860	820	760	685	590
	$\frac{d^2\sigma}{dp^2dw^2}$	8.0 ±1.0	7.4 ±0.7	8.2 ±0.7	8.0 ±0.7	7.2 ±0.6	3.7 ±0.4	3.0 ±0.3
τ_2	$\langle w \rangle =$	855	840	810	775	725	660	575
	$\frac{d^2\sigma}{dp^2dw^2}$	24.6 ±2.3	21.4 ±1.8	19.9 ±1.6	16.0 ±1.3	11.6 ±1.0	7.4 ±0.7	3.9 ±0.5
τ_3	$\langle w \rangle =$	815	800	775	740	695	635	560
	$\frac{d^2\sigma}{dp^2dw^2}$	20.4 ±3.1	18.3 ±2.1	20.6 ±1.8	17.3 ±1.5	11.7 ±1.1	7.3 ±0.8	4.4 ±0.7
τ_4	$\langle w \rangle =$	780	765	740	710	665	610	540
	$\frac{d^2\sigma}{dp^2dw^2}$	33.6 ±4.1	24.0 ±2.7	20.9 ±2.5	22.3 ±2.2	12.3 ±1.4	7.4 ±1.2	5.5 ±1.0
τ_5	$\langle w \rangle =$	735	725	705	675	635	585	520
	$\frac{d^2\sigma}{dp^2dw^2}$	31.2 ±5.1	22.4 ±3.3	26.6 ±3.0	16.1 ±2.3	11.4 ±1.7	8.8 ±1.4	5.2 ±1.1
τ_6	$\langle w \rangle =$	695	685	665	640	600	555	500
	$\frac{d^2\sigma}{dp^2dw^2}$	44.3 ±5.8	23.5 ±3.6	26.7 ±3.4	14.5 ±2.9	13.2 ±2.2	12.3 ±2.0	2.9 ±1.7
τ_7	$\langle w \rangle =$	650	640	625	600	565	525	475
	$\frac{d^2\sigma}{dp^2dw^2}$	37.5 ±8.3	20.4 ±4.8	21.6 ±4.4	10.6 ±4.1	10.1 ±2.8	7.5 ±2.4	3.2 ±2.1

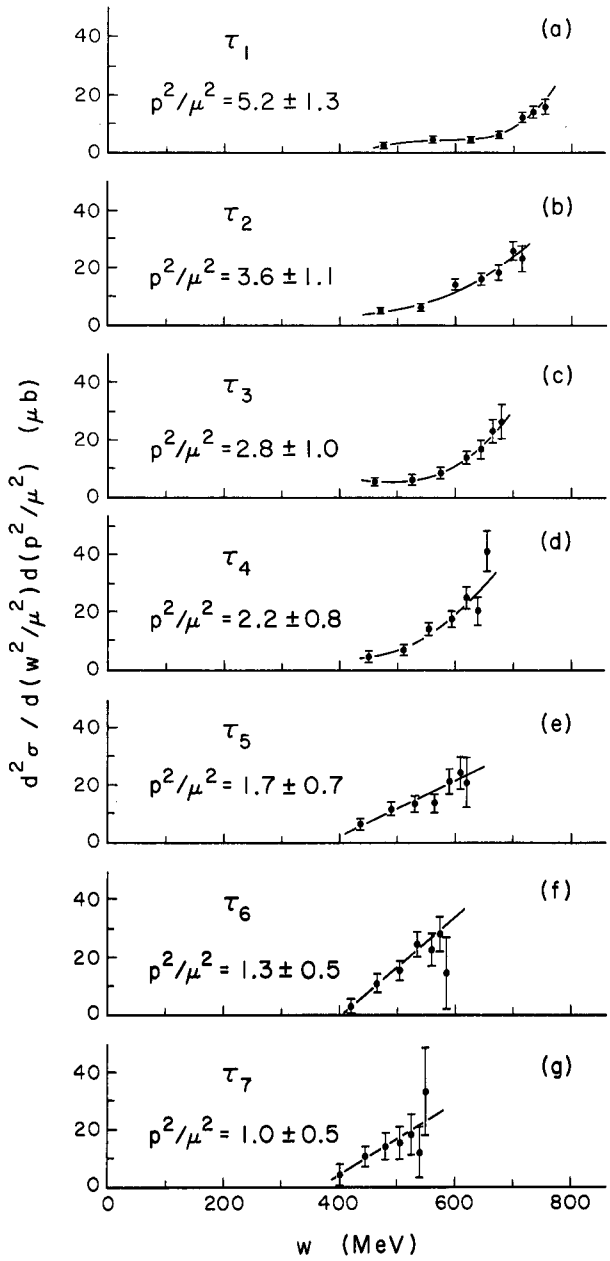

MUB-1649

Fig. 8. The partial cross section $d^2\sigma/d(w^2/\mu^2)d(p^2/\mu^2)$ is depicted as a function of w for an incident-pion momentum of 1.25 BeV/c. A separate plot is shown for time bins 1 through 7, respectively, in (a) through (g).

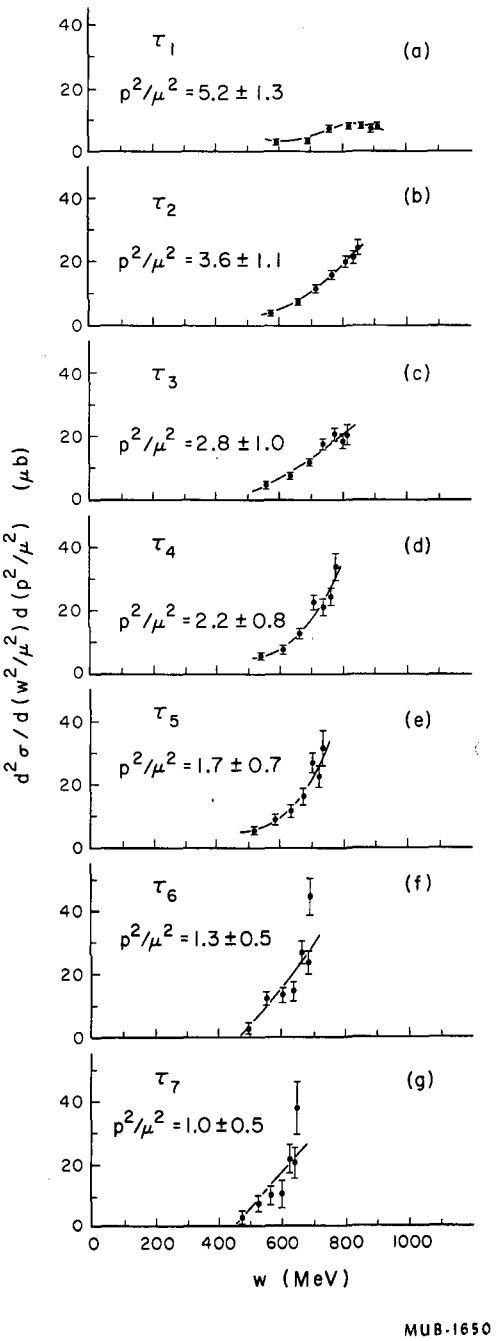

Fig. 9. The partial cross section $d^2\sigma/d(w^2/\mu^2)d(p^2/\mu^2)$ is depicted as a function of w for an incident-pion momentum of 1.75 BeV/c. A separate plot is shown for time bins 1 through 7, respectively, in (a) through (g).

IV. RESULTS AND CONCLUSIONS

Our data are examined below in an evolutionary order: first we make a simple study of the data's dependence on the variable w; next we obtain from the physical distributions the quantity defined in Sec. I as $\sigma_{12}(w^2)$; finally we turn to the extrapolation recipe given by Chew and Low and explore the reasons for its failure.

A. Structure of the Data in w

By studying the quantity $d\sigma/d(w^2)$ as a function of w we may infer some qualitative features about the pion-pion interaction. A comparison of this distribution with that predicted by phase space and normalized to the total cross section for $\pi^- + p \rightarrow \pi^+ + \pi^- + n$ gives two kinds of information. Peaking about a given w value implies an energy structure (perhaps a resonance) in the pion-pion system; also the magnitude of the cross section relative to the phase-space prediction gives a rough indication of the strength of the interaction. An enhancement over the phase space for low momentum transfers (the region of our measurement) is neatly explained by peripheral collisions of the incident pion with a virtual pion in the cloud surrounding the nucleon--i.e., there is a strong interaction between the two pions.

The distribution $d\sigma/d(w^2)$ was obtained from our double distribution data in the following way: for each of the seven p^2 intervals, the data were fitted in a least-squares sense to a polynomial in w^2. We chose the lowest-order polynomial that fit the data with reasonably high probability. (As remarked above, the solid curves shown in Figs. 8 and 9 represent these least-squares fits to the data.) From the fitted curve, the value of $d^2\sigma/d(p^2)d(w^2)$ was calculated for several integral values of w^2/μ^2; from the error matrix for the fitted curve the uncertainty in the double distribution was calculated[28] at these values of w^2. Then for a constant w value, the contributions from the seven p^2 intervals were integrated from the lowest p^2 allowed by kinematics to an upper cutoff at $p^2 = 6.5\,\mu^2$:

$$d\sigma/d(w^2) \equiv \int_{p^2_{min}(w^2)}^{6.5\,\mu^2} d^2\sigma/d(p^2)d(w^2)\; d(p^2) \,. \qquad \text{(IV-1)}$$

The uncertainties in each of the contributions were combined to form the total uncertainty in $d\sigma/d(w^2)$.

One can easily show that the double distributions predicted by a Lorentz-invariant phase space have the form

$$d^2\sigma/d(p^2)d(w^2) = (A/\mu^4)\,(1-4\mu^2/w^2)^{1/2} \,,$$

where A is a normalization parameter. Integration over p^2 according to Eq. (IV-1) yields

$$d\sigma/d(w^2)_{p.s.} = (A/\mu^4)\,(1-4\mu^2/w^2)^{1/2}[\,6.5\,\mu^2 - p^2_{min}(w^2)] \,. \qquad \text{(IV-2)}$$

Figures 10a and 10b show the distributions for incident momenta of 1.25 and 1.75 BeV/c, respectively. The solid curve represents the phase-space prediction normalized to a total cross section $\sigma(\pi^- p \to \pi^+ \pi^- n)$ of 10 mb. One notes in passing that the fitting procedures used to obtain $d\sigma/d(w^2)$ have smoothed the data considerably; the errors on the points no longer reflect independent standard deviations of normally distributed samples but rather indicate the uncertainty in points along a fitted curve.

There is a considerable enhancement over the phase-space prediction at both momenta, which suggests that peripheral collisions contribute significantly to our data. Further, the cross section $d\sigma/d(w^2)$ increases steeply with increasing w. At 1.75 BeV/c there seems to be a broad peak at $w \approx 750$ MeV; for 1.25 BeV/c the cutoff imposed in p^2 forces the cross section to zero at high w values and thus distorts the upper portion of the distribution. As we will see in the next section, where these kinematical factors are taken into account, the data at 1.25 BeV/c are rising steeply across the full range of w values explored by our experiment.

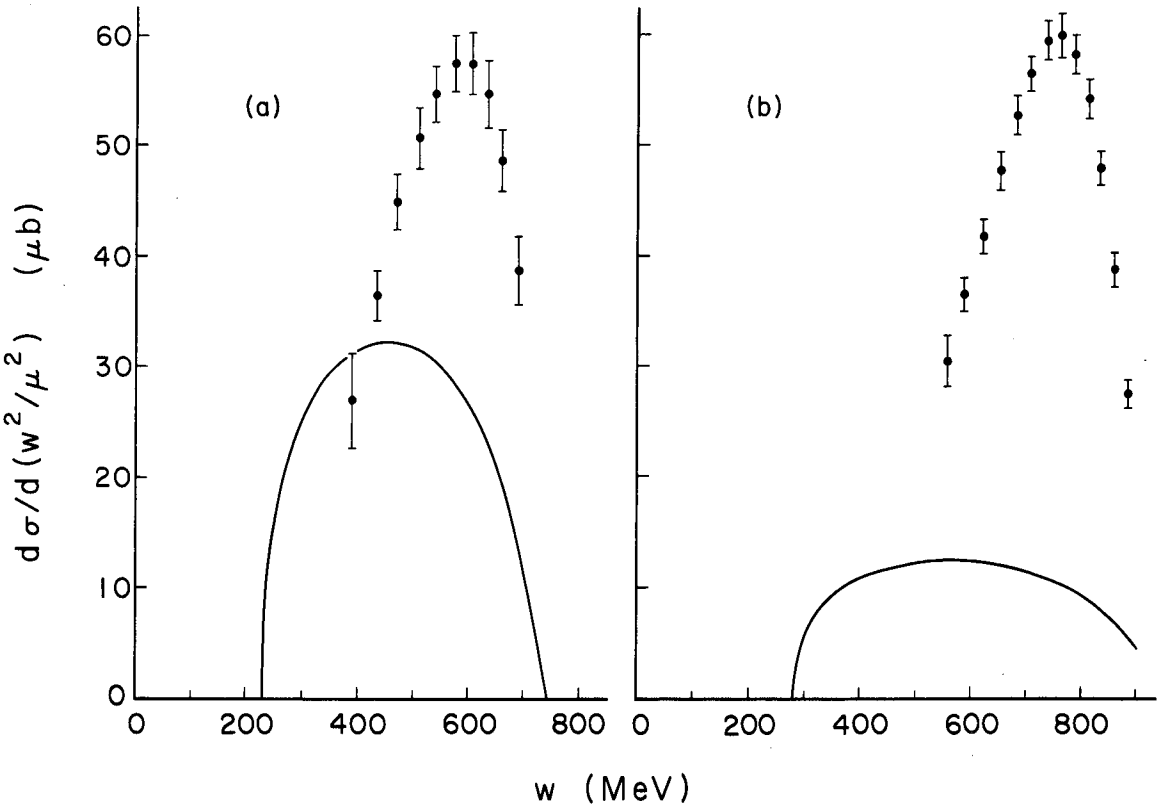

MUB-1651

Fig. 10. The partial cross section $d\sigma/d(w^2/\mu^2)$ vs w is shown in (a) for 1.25-BeV/c incident pions and in (b) for 1.75-BeV/c incident pions. The solid curves represent phase-space predictions normalized to a total cross section of 10 mb.

B. The w Structure After Removing Kinematical Factors

For the final state $(\pi^+\pi^-n)$, Eq. (I-4) reduces to

$$\frac{d^2\sigma}{d(p^2)d(w^2)} = \frac{f^2}{\pi} \frac{M_1^2}{M_2^2} \frac{(p^2/\mu^2)}{(p^2 - p_0^2)^2} \frac{(w^4/4 - w^2\mu^2)^{1/2}}{q_{1L}^2} \sigma_{12}(w^2) , \tag{IV-3}$$

where $\sigma_{12}(w^2)$ is the scattering cross section for a virtual pion incident on a physical pion and does not become the pion-pion cross section unless we continue the double distribution to the pole at $p^2 = p_0^2$. One should also recall that this formula includes only the contribution from the one-pion-exchange process. Keeping in mind these two serious limitations, we find it instructive to use Eq. (IV-3) to calculate pion-pion cross sections from our data.

We may use $d\sigma/d(w^2)$ obtained in the preceding section to accomplish this. Integrating Eq. (IV-3) according to the prescription of Eq. (IV-1) yields the relation

$$d\sigma/d(w^2) = \frac{f^2}{\pi} \frac{M_1^2}{M_2^2} \frac{H(w^2)}{q_{1L}^2} \sigma_{12}(w^2) , \tag{IV-4}$$

where

$$H(w^2) \equiv (w^4/4 - w^2\mu^2)^{1/2} \int_{p^2_{min}(w^2)}^{6.5\mu^2} \frac{(p^2/\mu^2)}{(p^2 - p_0^2)^2} d(p^2) . \tag{IV-5}$$

The dependence of $d\sigma/d(w^2)$ on w thus neatly divides into two parts--$H(w^2)$, which contains all kinematical factors, and $\sigma_{12}(w^2)$, which summarizes the effect of pion-pion interactions.

Figures 11a and 11b show the effect of removing these kinematical factors at 1.25 and 1.75 BeV/c; the quantity $\sigma_{12}(w^2)$ here depicted is defined through Eq. (IV-4). One sees again the characteristics

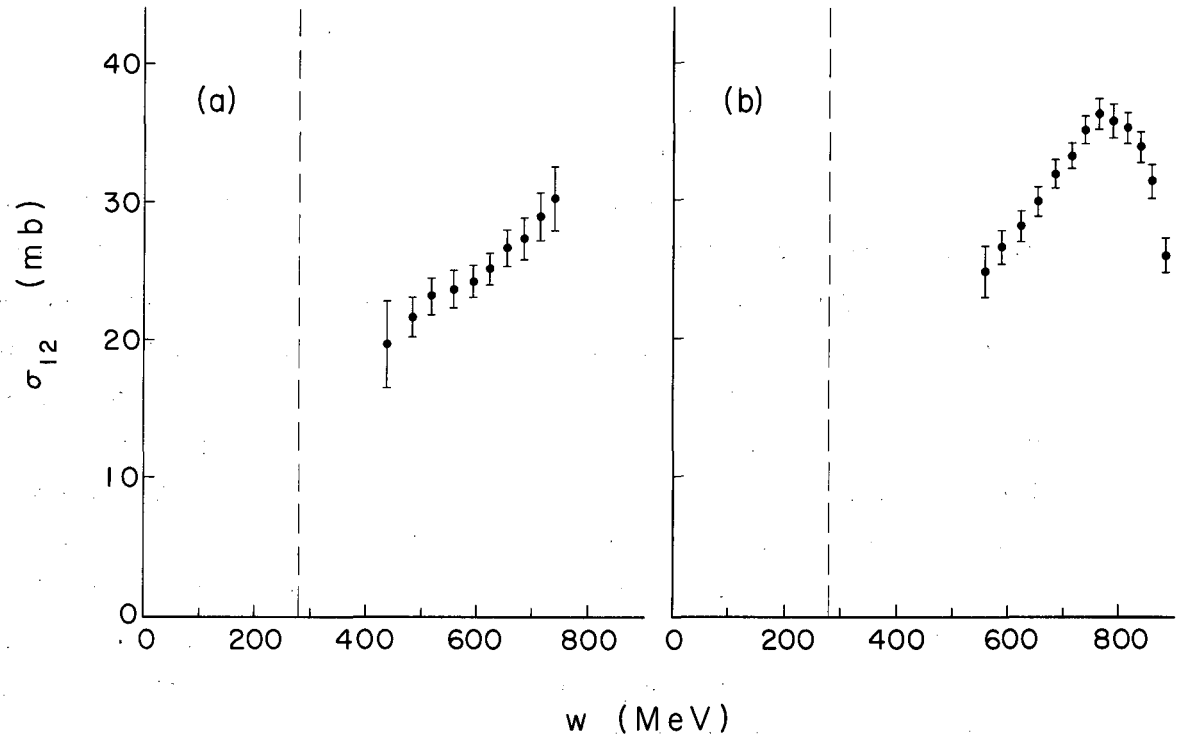

MUB-1652

Fig. 11. $\sigma_{12}(w)$, the pion-pion cross section derived from the double distributions $d^2\sigma/d(w^2/\mu^2)d(p^2/\mu^2)$ assuming one-pion exchange, is plotted vs w; (a) refers to 1.25-BeV/c incident pions, (b) to 1.75-BeV/c incident momentum. The dotted line designates the rest energy of the two-pion system.

described in Sec. IV-A: the 1.25- BeV/c data rise steeply toward increasing w values; at 1.75 BeV/c there is a broad peak centered between w = 700 and w = 800 MeV. The two curves agree rather well in the region of overlapping w values and are consistent with a resonance in the pion-pion system at w = 750 MeV.

C. The Effect of Finite Resolution

The position of the resonance indicated above is in good agreement with other experiments;[3-5] however, the width of our distribution is somewhat greater than that found in experiments at other incident momenta and with different charge combinations in the final state. It is of interest to determine whether the broadening we observe is instrumental. Once again we employ the Monte Carlo method. The application in this instance is quite simple: a large sample of neutrons was generated, by use of a computer program, according to a known distribution function in w^2 and p^2; the neutrons were then "detected" by the computer program in accordance with the measured energy-resolution functions of Sec. II and with the angular-resolution functions for Array I. A comparison of the known distribution function and the distribution as "seen" (via the computer program) by Array I yields the desired information about the resolution of the system.

The known distribution function used here was Eq. (IV-3) with a simple p-wave resonance form for $\sigma_{12}(w^2)$:

$$\sigma_{12}(w^2) = 12\pi \frac{\gamma^2(w^2 - 4\mu^2)^2/w^2}{(w^2 - w_R^2)^2 + \gamma^2(w^2 - 4\mu^2)^3/w^2} . \qquad \text{(IV-6)}$$

The parameters w_R and γ^2 determine the position and width of the resonance; in the present calculation a very narrow resonance (full-width at half maximum of approx 6 MeV) was generated at w = 750 MeV. From the resultant neutron distribution (generated by the Monte Carlo program) we calculated $d\sigma/d(w^2)$ in the same fashion as indicated above.

The effect of our finite resolution is shown in Fig. 12. The theoretical distribution $d\sigma/d(w^2)$ is given in Fig. 12a; the distribution as seen by our apparatus appears in Fig. 12b. We see that a distribution of negligible width is broadened to a full-width at half maximum of approximately 80 MeV. The high-energy "tails" on the neutron resolution functions (Sec. II-F) are primarily responsible for such broadening.

However, the width of the $d\sigma/d(w^2)$ distribution in Fig. 11b is not fully explained by finite resolution effects. The observed full-width at half maximum is approx 300 MeV, almost four times our basic resolution. The width reported in other experiments is approx 150 MeV (see Sec. I). If one repeats the Monte Carlo calculation outlined above with a resonance form $\sigma_{12}(w^2)$ having this width, the distribution, after broadening, appears to be approx 170 MeV wide. From this we conclude that the distributions we observe have significantly greater widths than those found in experiments at other incident momenta and with different charge states.

D. Extrapolation

From the double distributions $d^2\sigma/d(w^2)d(p^2)$ described above we can construct the extrapolation function $F(p^2, w^2)$ defined in Eq. (I-5). As in Sec. IV-A, the value of $d^2\sigma/d(w^2)d(p^2)$ at a given w value was obtained from the curves fitted to the data; the errors were calculated from the error matrix to the fitted curve.

For constant w we typically have the extrapolation function at seven values of p^2 appropriate to the seven flight-time intervals. For large w values there is a kinematical restriction on the range of p^2, and fewer than seven points appear on the extrapolation plots shown in Figs. 13 and 14. The value plotted is $F(p^2, w^2)/f^2$, where f^2 is the pion-nucleon coupling constant; from Sec. I we see

$$F(p_0{}^2, w^2)/f^2 = -\sigma_{\pi^+\pi^-}(w^2) . \qquad \text{(IV-7)}$$

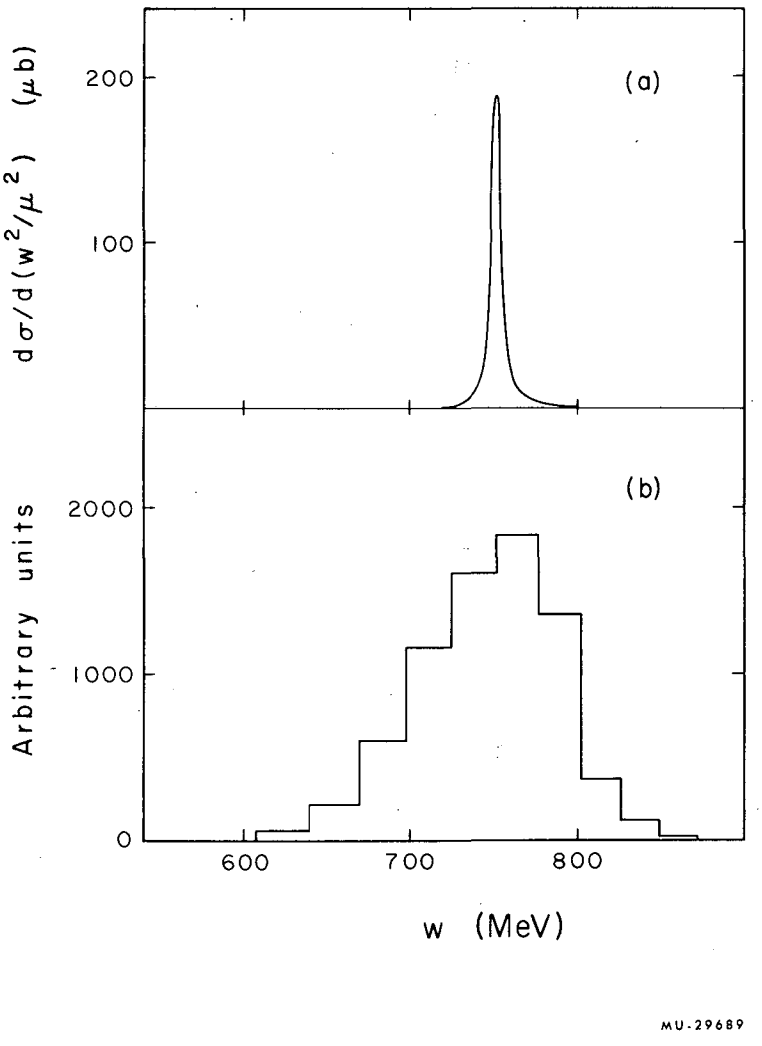

Fig. 12. Results of a Monte Carlo calculation performed to determine the resolution of our apparatus in w; (a) shows the distribution $d\sigma/d(w^2/\mu^2)$ according to which events were generated in the calculation; (b) shows the distribution as seen by our apparatus. Broadening is due to finite counter sizes and widths of the neutron flight-time intervals.

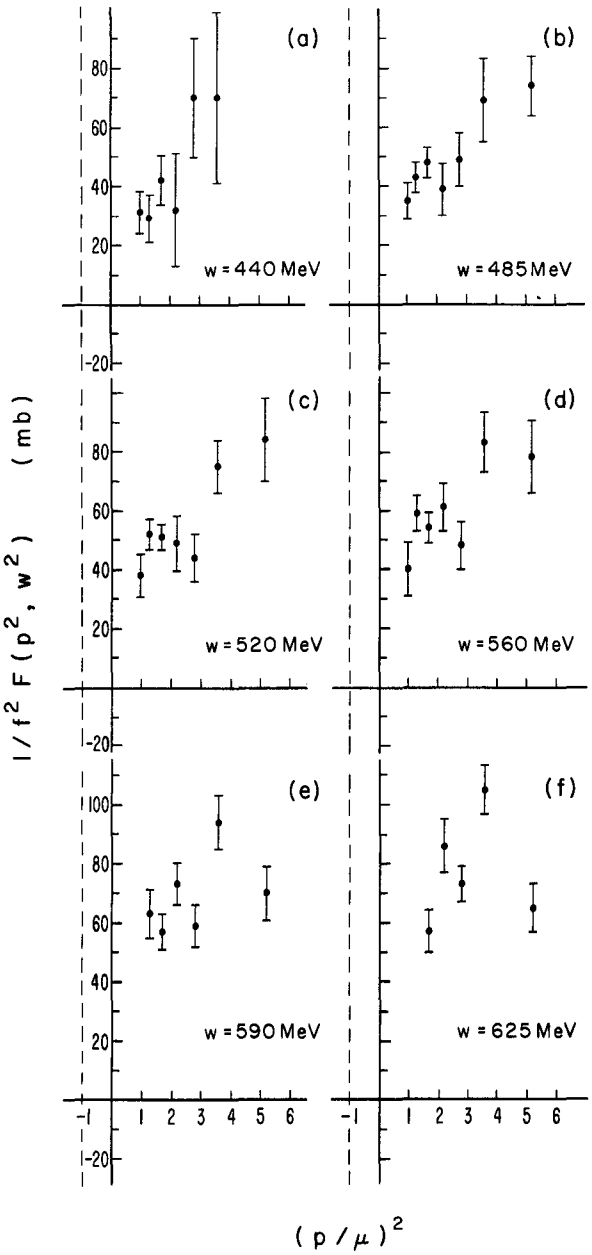

Fig. 13. Extrapolation plots for an incident momentum of 1.25 BeV/c. The dotted line indicates the value of f^2/μ^2 to which one must extrapolate $F(p^2, w^2)/f^2$ in order to obtain the physical pion-pion total cross section.

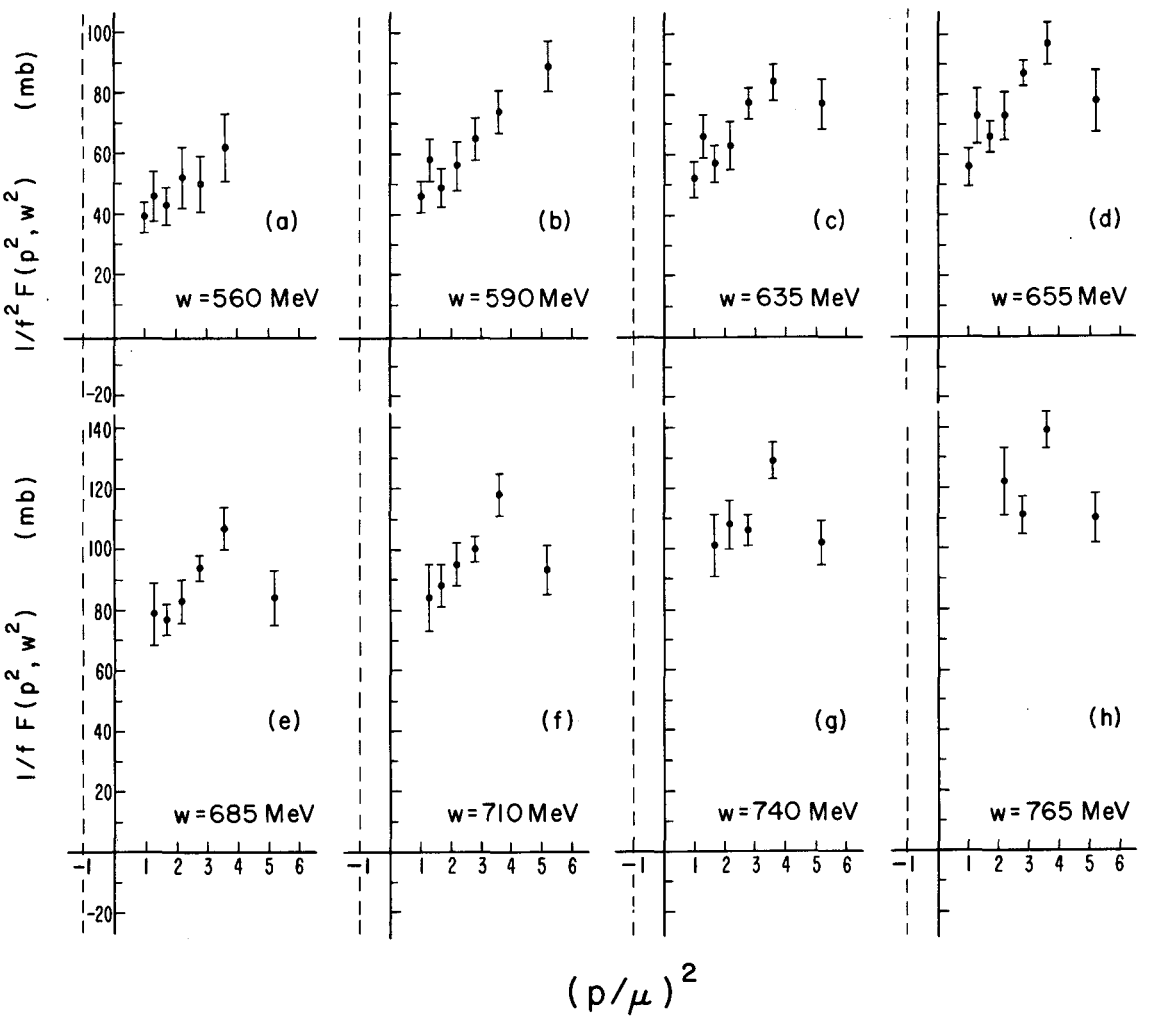

Fig. 14. Extrapolation plots for an incident momentum of 1.75 BeV/c. The dotted line indicates the value of p^2/μ^2 to which one must extrapolate $F(p^2, w^2)/f^2$ in order to obtain the physical pion-pion total cross section.

Upon examining the data, we find that, for low w values, $F(p^2, w^2)$ is approximately linear in p^2 within the statistical accuracy of the data. For larger values of w, the curves rise less steeply and fall off at high p^2. The value of the extrapolation function at the pole appears to be positive or in a few cases zero if one continues the curve linearly from the physical region. In light of Eq. (IV-7) this would indicate negative pion-pion cross sections--a physically untenable result.

Thus the extrapolation method, applied to our data, appears to fail. Such a failure indicates a breakdown of the assumptions on which the method is founded. Foremost among these is the assumption that one-pion-exchange processes dominate the interaction in the region of low momentum transfers. In the two sections following, we examine the data for evidence corroborating such deviations from one-pion exchange.

E. Final-State Pion-Nucleon Correlations

The three well-known resonances in the pion-nucleon system lead us to suspect a strong final-state interaction between the neutron and one of the pions. To study this possibility we invoke a method similar to that used by Dalitz in his analysis of τ-meson decays.[29] Pertinent to this method are two invariant quantities which we will call x and y:

$$x = (\omega_2 + \omega_{\pi 1})^2 - (\vec{p}_2 + \vec{p}_{\pi 1})^2$$

and (IV-8)

$$y = (\omega_2 + \omega_{\pi 2})^2 - (\vec{p}_2 + \vec{p}_{\pi 2})^2 .$$

Let the subscript $\pi 1$ denote the positive pion and $\pi 2$ the negative pion in our final state. Then x and y represent the square of the total energy in the π^+-n and π^--n systems, respectively. Though x and y are independent, four-momentum conservation restricts the range of their variation to an "egg-shaped" region of x-y space. Figures 15a and 15b depict this region for incident momenta of 1.25 BeV/c and 1.75 BeV/c respectively. A simple calculation shows that each element of area dxdy

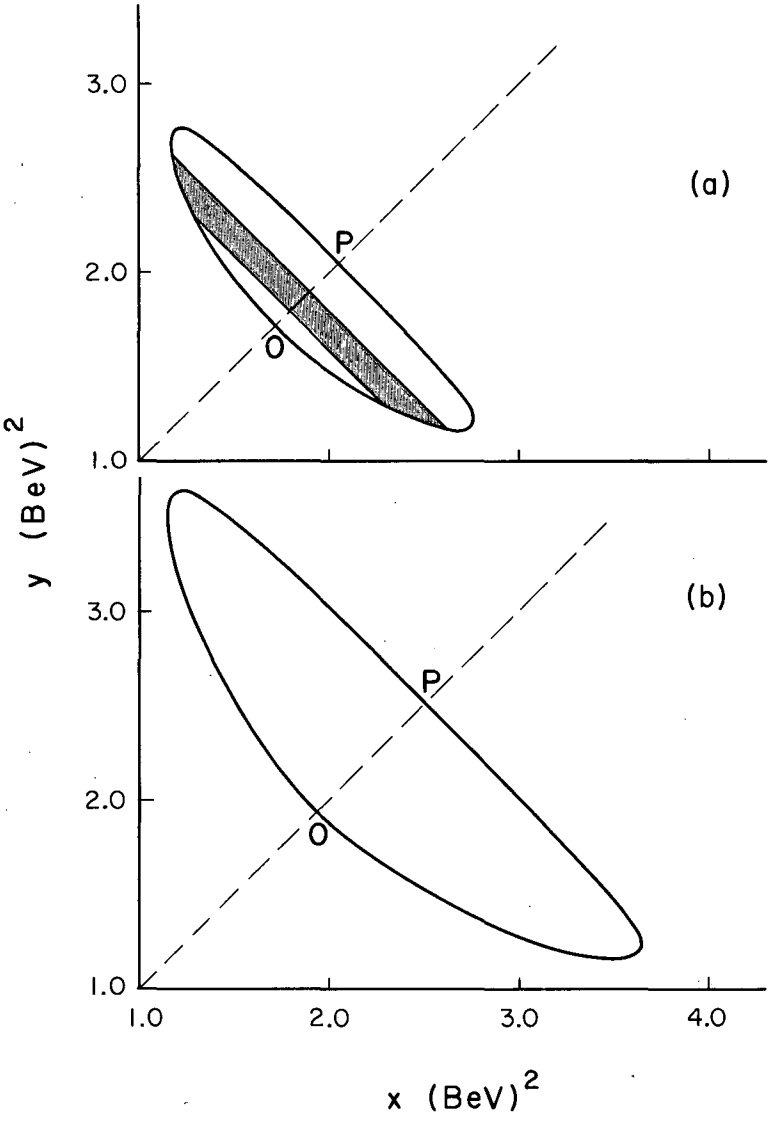

Fig. 15. Dalitz plot ovals for the pion-neutron final-state systems in $\pi^- + p \rightarrow \pi^- + \pi^+ + n$ for (a) 1.25 BeV/c incident-pion momentum, and (b) 1.75 BeV/c incident-pion momentum.

within the "egg" has equal weight in phase space; if the interaction has a constant matrix element, the "egg" must be uniformly populated with events; and conversely any dependence of the interaction on x and y appears as a clustering of events inside the "egg".

Four-momentum conservation yields a simple linear relationship between x, y, and w^2:

$$x + y + w^2 = 2\mu^2 + M_n^2 + (\omega_{1L} + M_p)^2 - q_{1L}^2 . \qquad \text{(IV-9)}$$

Thus each value of w^2 defines a line with unit slope in x-y space. A band of w values $w_0 \pm \Delta w$ maps into a diagonal strip cutting across the "egg"; an example of this is the darkened region of Fig. 15a. If the distribution of events inside the "egg" follows phase space, the population of events in such a strip as a function of the variable x must be proportional to the width of the strip in y and, except near the boundaries of the "egg", will be flat. Imposing an upper cutoff in the momentum-transfer variable Δ^2 (or equivalently in p^2) does not alter this flat distribution as long as the width of the w strip is sufficiently narrow.

We have assumed above that the charges of the final-state pions are experimentally observed. This is not the case in our experiment, and the following symmetry is imposed: since we cannot distinguish x and y, we must plot each event twice--a procedure which symmetrizes the population of the "egg" about the diagonal line OP in Fig. 16. The density of events projected along the x axis must be identical with the density distribution projected along the y axis.

To apply this type of analysis to our data, use was made of the master-packed data tapes described in Sec. III-A. A computer program scanned these tapes and calculated x, y, and w^2 for each event. At 1.25 BeV/c three w strips were chosen: 440 to 650 MeV, 650 to 725 MeV, and 725 to 800 MeV. The large number of events at 1.75 BeV/c allowed selection of five w strips: 480 to 625 MeV, 625 to 700 MeV, 700 to 765 MeV, 765 to 825 MeV, and finally 825 to 900 MeV. On the basis of w^2, the appropriate w strip was selected; for each such strip,

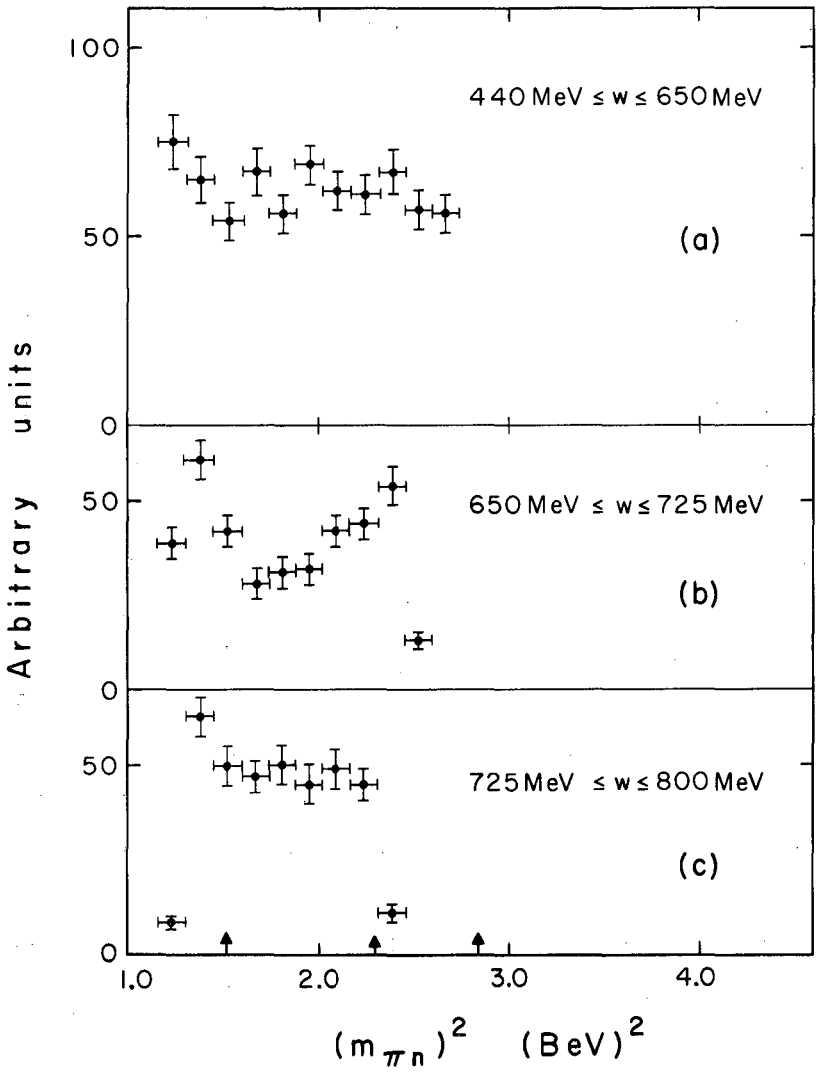

Fig. 16. Distribution of events as a function of the square of the mass of the pion-neutron system in various w intervals for 1.25 BeV/c incident momentum. Arrows indicate the positions of known pion-nucleon resonances.

the range of x and y was divided into bins. The values of x and y determined which two bins (since each event was plotted twice) were to be incremented. To account for neutron-counting efficiencies, an average detection efficiency was assigned to each flight-time interval, and the bins were incremented by the reciprocal of this efficiency. A separate tally was kept for each target and delay condition so that subtractions could be performed in accordance with Eq. II-3). Thus, for each w strip, we prepared the projected density distribution described above. Figures 16 and 17 show these distributions for 1.25 and 1.75 BeV/c, respectively. The positions of the known pion-nucleon resonances are marked by arrows.

In the data at 1.25 BeV/c a strong pion-nucleon correlation near the first and second resonances appears in the second w strip. No appreciable correlation appears in the other two w strips. That no deviation from a flat distribution occurs for low w values may have a kinematic explanation: lower momentum transfers Δ^2 are kinematically allowed as one decreases w. For small Δ^2 one-pion-exchange processes may tend to dominate the pion-nucleon final-state interaction as indicated in Sec. I. The flat distribution found in the third w strip may be due to the strong pion-pion interaction for these w values; one might expect that interference between the two processes would distort their separate resonant characters. Also the range of pion-nucleon mass values is kinematically restricted for large w, and edge effects at the boundaries of the "egg" (see Fig. 16a) distort the extremities of the mass-value spectrum.

At 1.75 BeV/c a strong correlation is observed around the first and third pion-nucleon resonances at w values above the dipion resonance; the distributions below w = 825 MeV are flat within statistics.

The presence of these correlations in the π-n systems is a clear indication of deviation from the one-pion-exchange model.

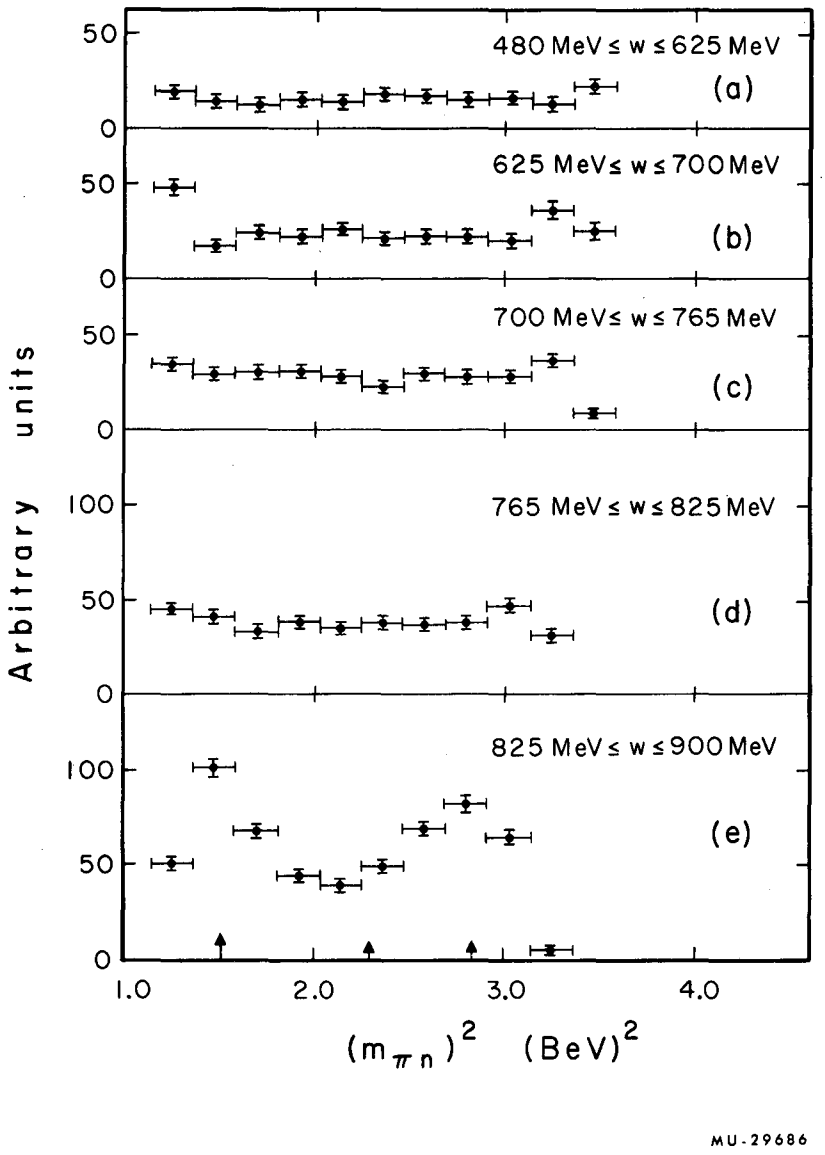

Fig. 17. Distribution of events as a function of the square of the mass of the pion-neutron system in various w intervals for 1.75 BeV/c incident momentum. Arrows indicate the positions of known pion-nucleon resonances.

F. Treiman-Yang Test

Treiman and Yang have proposed a test to detect deviations from the one-pion-exchange model.[30] The test exploits the scalar nature of pions--they carry no spin angular momentum. In the one-pion-exchange process (see Fig. 1) we assume that a single virtual pion is exchanged between the pion-nucleon vertex and the pion-pion vertex (A and B respectively in Fig. 1). Suppose we make a transformation into the rest frame of the incident pion; let $\vec{q}$ be the three-momentum of the virtual pion as it impinges on the pion at rest. Since the virtual pion is spinless, there can be no azimuthal dependence in the differential scattering cross section of the two pions--i.e., the cross section is invariant under rotations about $\vec{q}$.

To state this mathematically, we introduce the following quantities, all measured in the rest frame of the incident π meson: let $\vec{p}_1$ and $\vec{p}_2$ be the three-momenta of the target proton and recoil neutron, respectively, let $\vec{q}$ (as above) be the momentum of the virtual pion, and let $\vec{k}_1$ and $\vec{k}_2$ be the three-momenta of the final-state pions. We introduce the basis set of unit vectors

$$\hat{i} = (\vec{p}_1 \times \vec{p}_2)/\left|\vec{p}_1 \times \vec{p}_2\right|,$$
$$\hat{j} = \vec{q} \times (\vec{p}_1 \times \vec{p}_2)/\left|\vec{q} \times (\vec{p}_1 \times \vec{p}_2)\right|, \qquad \text{(IV-10)}$$

and

$$\hat{k} = \vec{q}/\left|\vec{q}\right|.$$

The unit normal to the pion-pion scattering plane is given by

$$\hat{n} = (\vec{k}_1 \times \vec{k}_2)/\left|\vec{k}_1 \times \vec{k}_2\right|. \qquad \text{(IV-11)}$$

The azimuthal scattering angle ϕ is then uniquely defined by the equations

$$\cos\phi = (\hat{i} \cdot \hat{n})$$

and $\qquad \text{(IV-12)}$

$$\sin\phi = (\hat{j} \cdot \hat{n}).$$

Validity of the one-pion-exchange model requires that the distribution of events be isotropic with respect to ϕ. Other processes need not give isotropy. The test is a negative one in that isotropy does not ensure one-pion exchange, whereas anisotropy gives clear evidence for deviations from this model.

Our inability to distinguish the charges of the final-state pions once again imposes a symmetry condition for application to our data. If we cannot distinguish $\vec{k}_1$ from $\vec{k}_2$, our distributions must be symmetric under the transformation $\hat{n} \rightarrow -\hat{n}$, or equivalently,

$$\begin{cases} \cos\phi \rightarrow -\cos\phi\,, \\ \sin\phi \rightarrow -\sin\phi\,. \end{cases} \qquad \text{(IV-13)}$$

Thus ϕ is uniquely defined only in the range from 0 to 180 deg.

In performing this test on our data, we once again used the master-packed data tapes. A computer program calculated ϕ for each event. A separate distribution in ϕ was made for each flight-time interval so that no knowledge of neutron counting efficiency was required. The necessary subtractions were performed for the various target and delay conditions. The resultant distributions are shown in Figs. 18 and 19.

In the 1.75-BeV/c data (Fig. 19) there is a significant deviation from isotropy in the first two flight-time intervals. For other time bins, the distributions are flat within statistics. The data for 1.25 BeV/c show similar tendencies but with poorer statistical accuracy.

It should be pointed out that our symmetry condition seriously impairs the sensitivity of the test. Treiman and Yang suggest that the first deviations from isotropy would be proportional to $\cos\phi$. The symmetry of our data about $\phi = 180$ deg makes it impossible for us to observe these first-order effects. The deviations we see must be proportional at least to $\cos^2\phi$ in order to survive the symmetry restriction. If the deviations from isotropy occur in the order suggested by Treiman and Yang, the anisotropy we observe may indeed indicate very serious deviations from one-pion exchange.

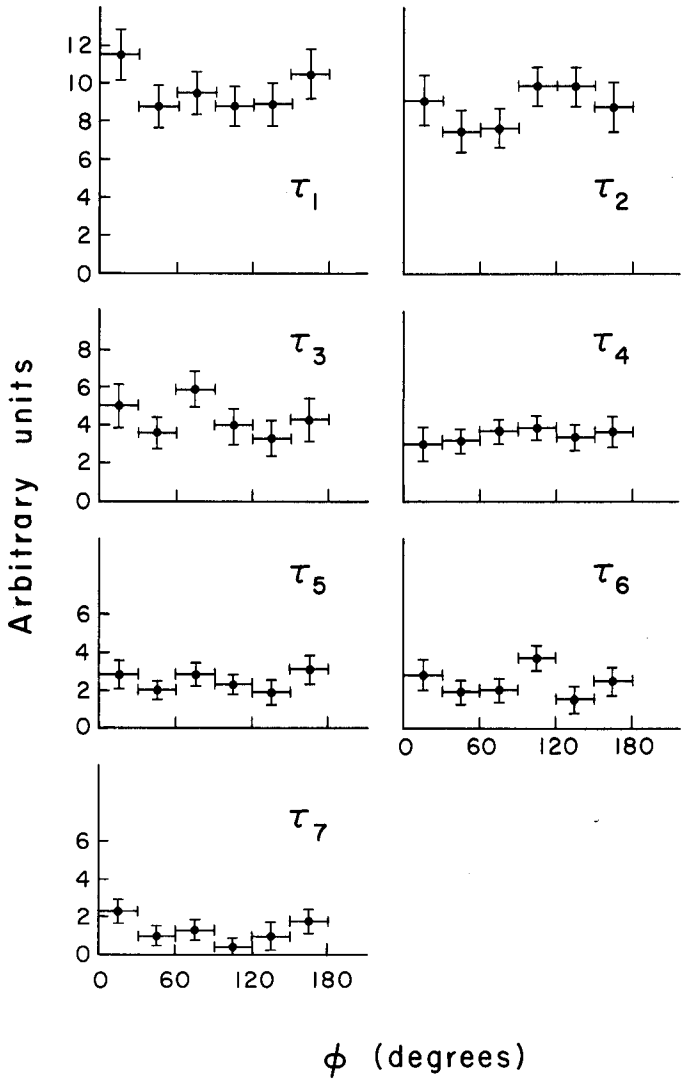

Fig. 18. Distribution of events in the Yang-Treiman angle ϕ (see text for definition) for each neutron flight-time interval. The incident-pion momentum is 1.25 BeV/c.

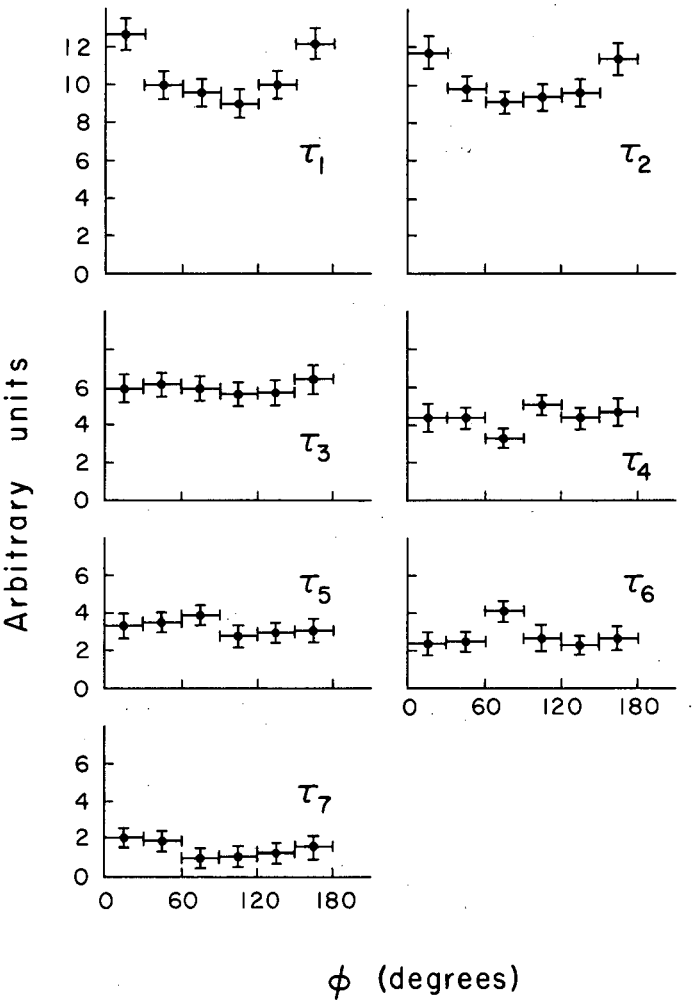

Fig. 19. Distribution of events in the Yang-Treiman angle ϕ (see text for definition) for each neutron flight-time interval. The incident-pion momentum is 1.75 BeV/c.

G. Conclusions

The results of this experiment seem indicative of two things.

First, our data tend to corroborate the existence of a pion-pion resonance at $w = 750$ MeV. From this experiment and another performed with the same apparatus studying the process

$$\pi^+ + p \rightarrow \pi^+ + \pi^+ + n, \qquad \text{(IV-14)}$$

we can limit the value of isotopic spin associated with the resonance. The experiment studying the reaction of Eq. (IV-14) showed no comparable resonant state.[31] Since the π^+-π^+ system is pure $I = 2$, the resonance we observe is restricted to $I = 1$ or 0. Our inability to distinguish the charges of the final-state pions makes it very difficult to ascertain the spin state of the resonance or obtain differential cross sections for the pion-pion system. However, our results are certainly compatible with and tend to corroborate the existence of the $I = 1$, $J = 1$ resonance observed in other experiments and known in the literature as the ρ meson.

In addition, we find considerable evidence for processes other than one-pion exchange: the pion-nucleon resonance correlations show specific evidence of a final-state interaction; the Treiman-Yang test gives general indication of other processes. The presence of such processes is probably responsible for the rather large width we find in our $d\sigma/d(w^2)$ distributions. It may also be significant that the resonance widths observed in other experiments are not in precise agreement. From the "Uncertainty Principle" we may estimate the lifetime of a particle with an energy width of 150 MeV to be

$$\Delta t \approx \frac{\hbar}{\Delta E} = 4.4 \times 10^{-24} \text{ sec.}$$

Traveling at the velocity of light, such a particle moves approximately one pion Compton wave length on the average before decaying. The decay products are thus in close proximity to the interaction center where the particle was produced--a situation conducive to final-state interactions. Depending on the strength of these interactions, the energy width associated with the particle's decay may vary.

In light of these considerations, the failure of our data to extrapolate according to the prescription of Chew and Low is somewhat less puzzling. Indeed, it is important to realize the limitations of the extrapolation method; its failure here points out the need for more powerful techniques of extracting from the data information about pion-pion interactions.

ACKNOWLEDGMENTS

I wish to express my indebtedness to my co-workers on this experiment: Dr. Joseph Lach, Dr. Leonard Auerbach, Dr. Tom Elioff, Dr. Thomas Ypsilantis, and Dr. Clyde Wiegand. Their intense interest, unflagging assistance, and good company were vital in supporting this experiment through the many long months of its existence. Especial thanks are due to Doctor Wiegand for his numerous innovations in the design of the counter arrays and electronic apparatus, and to Doctor Ypsilantis, who suggested this research project to me and continually guided it to completion.

I futher wish to acknowledge the contribution of the two supporting electronics groups: Mr. Quentin Kerns, Mr. Thomas Nunamaker, and Mr. Arthur Bjerke, who built and maintained the Chronotron; and Mr. Fred Kirsten and Mr. Stanley Baker, who designed and kept in operation the data-storage and magnetic-tape equipment.

Dr. Geoffrey Chew contributed many valuable discussions concerning the theoretical aspects of the experiment.

Mr. Joseph Good deserves special mention for his considerable help with the coding and computer problems encountered in analyzing the data.

The operating crews of both the Bevatron and 184-inch cyclotron are to be thanked for their co-operation and assistance.

Special thanks are due to Dr. Edwin McMillan for his continued interest and his intriguing cryptograms.

And finally I wish to acknowledge Dr. Herbert Steiner's considerable assistance during the early stages of the experiment and Dr. Emilio Segrè's numerous discussions and valued support throughout the experiment.

APPENDIX

A. Formulae Used in Kinematical Fitting

To define more succinctly the functions Θ and $\underline{\phi}$ of Sec. III-B, we introduce the quantities

$$m^2 = (M_2^2 + \mu_1^2 + \mu^2 + M_1^2 - \mu_2^2)/2 ,$$

$$\cos\eta = \cos\theta_2 \cos\theta_{\pi 1} + \sin\theta_2 \sin\theta_{\pi 1} \cos\phi_{\pi 1} ,$$

$$r = (q_{1L} \cos\theta_{\pi 1} - p_2 \cos\eta)/\mu ,$$

$$s = (m^2 - \omega_2 M_1 - \omega_2 \omega_{1L} + M_1 \omega_{1L} + q_{1L} p_2 \cos\theta_2)/\mu^2$$

and

$$t = (\omega_{1L} + M_1 - \omega_2)/\mu . \qquad \text{(A-1)}$$

The momentum $p_{\pi 1}$ is related to r, s, and t by

$$p_{\pi 1} = \frac{-rs \pm [(\mu_1/\mu)^2(r^2 - t^2) + s^2]^{1/2}}{(r^2 - t^2)} . \qquad \text{(A-2)}$$

From $p_{\pi 1}$ we may calculate $\omega_{\pi 1} = (p_{\pi 1}^2 + \mu_1^2)^{1/2}$ and obtain $\omega_{\pi 2}$ from energy conservation:

$$\omega_{\pi 2} = \omega_{1L} + M_1 - \omega_2 - \omega_{\pi 1}$$

and

$$p_{\pi 2} = (\omega_{\pi 2}^2 - \mu_2^2)^{1/2} . \qquad \text{(A-3)}$$

We are now ready to define Θ and $\underline{\phi}$:

$$\Theta = \cos^{-1}\left[\frac{q_{1L} - p_{\pi 1}\cos\theta_{\pi 1} - p_2 \cos\theta_2}{p_{\pi 2}}\right]$$

and

$$\underline{\phi} = \tan^{-1}\left[\frac{p_{\pi 1} \sin\theta_{\pi 1} \sin\phi_{\pi 1}}{p_{\pi 1} \sin\theta_{\pi 1} \cos\phi_{\pi 1} + p_2 \sin\theta_2}\right] . \qquad \text{(A-4)}$$

Since the arctangent is defined only in the interval from zero to 180 deg, we need further information to complete the definition of $\underline{\phi}$:

$$\sin \underline{\overline{\phi}} = \frac{-p_{\pi 1} \sin \theta_{\pi 1} \sin \phi_{\pi 1}}{p_{\pi 2} \sin \Theta} \quad . \tag{A-5}$$

From the algebraic sign of $\sin \underline{\overline{\phi}}$ we can now select the proper quadrant for the angle $\underline{\overline{\phi}}$.

One readily sees that the functions Θ and $\underline{\overline{\phi}}$ are algebraically complicated. This, however, poses no special problem for an electronic computer: the only difficulty arises from the sign ambiguity in Eq. (A-2). If two nonnegative values can be found for $p_{\pi 1}$, the fitting program must follow both alternatives. Though this seldom occurs, the possibility must be taken into account in the coding of the program.

There is also a possibility that no physical values of $p_{\pi 1}$ exist for a particular choice of the defining set of variables. This may come about in two ways: the quantity inside the radical in Eq. (A-2) may be negative, or both choices of the sign before the radical may lead to negative momenta. When this situation arose, a subsearch of the defining set was conducted by the fitting program to obtain physical momenta. The path of the subsearch was guided by appropriate gradients and resembled in logic the search to fulfill the fitting criterion. If no physical momenta could be found in a preset number of search steps, the event was rejected.

B. The Monte Carlo Method

1. The General Problem

Often one must deal with complicated systems whose separate components are individually well understood. To study the operation of such a system sometimes presents serious computational problems. An exact solution, though possible in principle, may be prohibitively difficult in practice. In such a situation it may be expedient to resort to the so-called Monte Carlo method of calculation, whose answers, though not in closed form, represent a solution to the problem in a statistical sense. The approach is simple: the entire system is mocked

up mathematically and trial events are followed through the system in detail. The operation of each component is generated in a statistical manner. The result of a large number of such trial events yields a statistically valid solution to the function of the system as a totality.

The operation of each component of the system must be stated as a statistical law. Let x be the outcome of a trial event passing through a given component (x might be the scattering angle of a neutron after colliding with a proton, for example); let $P(x)dx$ be the probability of obtaining a value of x between x and $x + dx$. We then construct the function $R(x)$:

$$R(x) = \int_{x_{min}}^{x} P(y)\, dy, \tag{B-1}$$

where $R(x)$ is monotonically increasing in the interval $x_{min} \leq x \leq x_{max}$, where x_{min} and x_{max} are the lower and upper limits imposed on the variable x. Conservation of probability requires

$$R(x_{max}) = 1 . \tag{B-2}$$

From a well-known theorem of the calculus,[32]

$$R'(x) = \frac{d}{dx} R(x) = P(x) . \tag{B-3}$$

Suppose we now generate random numbers in the interval from zero to one. Let us associate with each random number n a value x_0 in accordance with the equation

$$n = R(x_0) . \tag{B-4}$$

If we generate N such random numbers, the population of numbers in the interval between n and $n + dn$ is simply $N\, dn$:

$$N\, dn = N\, (dn/dx)\, dx = NR'(x_0)dx = N\, P(x_0)\, dx, \tag{B-5}$$

just the result expected if one populated the entire interval in x with N events distributed according to $P(x)$. Thus, if we associate each random number n with a value x_0 according to Eq. (B-4), we obtain the required distribution of the variable x.

The cyclic nature of the Monte Carlo method (following trial events through a system) is well suited to programming for an electronic computer. All the Monte Carlo calculations described in the text were done by use of an IBM 709 computer. In writing such programs we found it useful to make each component of the system under study a separate subprogram (subroutine) which, given n, solves Eq. (B-4) for x_0. Each component may then be tested separately to confirm that it generates the correct distribution for x. Additionally, such subprograms are then easily interchangeable for use in other Monte Carlo calculations. Once all the subprograms are functioning properly, one writes a main program which orders the subprograms in the same way as the system being studied.

It is often useful, if R(x) is sufficiently transcendental, to prepare a table of the values of R(x) at the beginning of the Monte Carlo calculation. The subprogram dealing with R(x) then solves Eq. (B-4) by bracketing n between two entries in the table. Linear interpolation between these entries usually yields x_0 with fully adequate accuracy. This technique is often easier than iterative methods of solving Eq. (B-4); but the main advantage is speed: most computers are equipped with logical instructions designed expressly for examining tables; the time required for these instructions is typically a small fraction of that needed in arithmetic operations.

The source of random numbers used in performing a Monte Carlo calculation requires considerable attention. When using a computer one usually resorts to a so-called pseudorandom number generator, which consists of a subprogram initially containing a "seed" or generating number. Successive numbers are formed from this "seed" by various operations: one method squares the "seed" (yielding a number with twice as many positions) and takes the central digits of the square; another method performs successive shift and add operations on the "seed." The new number, though not truly random, is very weakly correlated to

its predecessor; it replaces the old "seed" for generating future numbers and is returned by the subprogram, after proper normalization, as a "random" number. Such a generator is necessarily cyclic: even if the digits of the new number were perfectly random, there is a finite probability of generating the original "seed" again and thus restoring the generator to its initial configuration; also a zero may be generated, which thereafter produces nothing but zeros. The choice of the initial "seed" is thus important; one tries to select a number whose cyclic properties have a very large period.

In addition to these difficulties, pseudorandom numbers often contain subtle and annoying correlations. These depend on the "seed" and the method of generation and are difficult to predict in advance. It is advisable to subject such a generator to rigorous testing (generating numbers in the same quantity, order, and range as required in the Monte Carlo calculation) before putting it into use. Such correlations usually appear as statistical discontinuities in the results of the calculation and fortunately can be discovered.

2. The Pion-Scattering Calculation

The pion-scattering correction discussed in Sec. III-E provides a pertinent elementary example of this method; consider the problem posed in hypothesis II: pions scattering in carbon in a typical element of Array I, given a total cross section of 250 mb, the angular distribution measured by Abbattista et al.,[25] and a multiplicity of one.

Two subprograms were required. The first determined on the basis of a random number n_1 whether a pion scattered in traversing a length L of scintillation material. Since the cross section was assumed constant in our hypothesis, we can easily calculate the probability of scattering to be

$$p = 1 - e^{-N\sigma} , \qquad \text{(B-6)}$$

where N is the number of carbon nuclei per square centimeter in a

length L of scintillator, and σ is the scattering cross section. Scattering is said to occur whenever $n_1 \leq p$.

The second subprogram selected scattering angles according to the data of Abbattista et al. Their angular distribution was integrated, normalized to one, and incorporated into a table as suggested in the previous discussion; the argument of the table was the cosine of the polar scattering angle. A second random number n_2 was then bracketed between entries in this table and a linear extrapolation used to obtain the corresponding value of cos θ. Since the distribution must be azimuthally symmetric, the azimuthal scattering angle ϕ was selected as

$$\phi = n_3(360) \text{ deg},$$

where n_3 was a third random number.

The main program that employed these subroutines established the geometry of the system, ordered the logic of the calculation, and kept a tally of the results.

The geometrical shape of the counters was slightly simplified to facilitate the calculation: the azimuthal and polar boundaries of the counter were taken to be arcs rather than chords. Thus the pion was taken to be inside the counter whenever its polar coordinates R, θ, and ϕ relative to the center of the hydrogen target obeyed the inequalities

$$160 \text{ cm} \leq R \leq 175 \text{ cm},$$

$$\theta_{\text{lower}} \leq \theta \leq \theta_{\text{upper}},$$

and

$$-15 \text{ deg} \leq \phi \leq 15 \text{ deg}, \qquad \text{(B-7)}$$

where θ_{lower} and θ_{upper} are the polar angle limits appropriate to the θ ring under consideration.

The main program began the calculation by choosing the initial coordinates of the pion to be

$$R = 160 \text{ cm},$$

$$\cos\theta = \cos\theta_{\text{upper}} + (\cos\theta_{\text{lower}} - \cos\theta_{\text{upper}}) \times n_\theta,$$

and

$$\phi = -15 + (15) \times n_\phi \text{ deg}, \qquad \text{(B-8)}$$

where n_θ and n_ϕ are two random numbers. This choice uniformly illuminates the surface of the counter with pions. The initial trajectory of the pion was taken to be radial. The program accounted for plural scattering by stepping along the trajectory in small increments, each of length L; after each step the first subprogram was consulted to ascertain whether scattering had occured. If the pion scattered, the second subprogram was addressed to obtain the scattering angles; from these the main program calculated the trajectory after scattering. Successive steps were then taken along the new trajectory until the pion violated the inequalities of Eq. (B-7) and thus passed out of the counter.

If the first inequality were violated, the pion was recorded only in the counter upon which it was incident. If either of the remaining inequalities were violated, at least one adjacent counter would have registered a count. The main program kept a tally of this latter class of events. The desired correction is simply the fraction of the total number of events comprised by this class.

3. Neutron-Rescattering Correction

The logic of the neutron-rescattering calculation is covered in the main body of the text. Two points, however, deserve special attention: treatment of the neutron-proton differential cross sections and the estimate of error introduced by the Monte Carlo method.

Since the calculation required knowledge of n-p scattering as a function of both energy and scattering angle, a two-variable fit was made to the data summarized by Hess.[17] The fitting was done in two steps. At each energy from zero to 130 MeV, where an angular distribution had been measured, the differential cross section in the barycentric frame was fitted in a least-square sense to the form

$$d\sigma/d\Omega^* = A(T_i) + B(T_i) \cos \theta^* + C(T_i) \cos^2 \theta^*, \qquad \text{(B-9)}$$

where θ^* is the barycentric-frame scattering angle and T_i is the kinetic energy of the incident neutron in the laboratory frame. The

coefficients $A(T_i)$, $B(T_i)$, and $C(T_i)$ thus obtained were then fitted as functions of energy. The n-p system has a well-known bound state (the deuteron) and a large $^1S_0$ scattering length; this leads us to expect (at least in the zero-range approximation) two simple poles in $A(T_i)$ occurring at $T_i = -2.2$ MeV and at $T_i = -0.06$ MeV.[33] To facilitate fitting, these singularities were removed by constructing the function $D(T_i)$:

$$\begin{aligned} D(T_i) &\equiv (T_i + 2.2)\,(T_i + 0.06)\,A(T_i) \\ &= d_0 + d_1 T_i + d_2 T_i^{\,2} + d_3 T_i^{\,3} . \end{aligned} \tag{B-10}$$

Solving for $A(T_i)$, we then obtain

$$A(T_i) = \frac{d_0 + d_1 T_i + d_2 T_i^{\,2} + d_3 T_i^{\,3}}{(T_i + 2.2)\,(T_i + 0.06)} \quad ; \tag{B-11}$$

the order of the polynomial indicated in Eqs. (B-10) and (B-11) (cubic) seemed to yield the best fit to the data. Adequate fits for $B(T_i)$ and $C(T_i)$ were obtained by using a quadratic and a quartic form, respectively:

$$\begin{aligned} B(T_i) &= b_0 + b_1 T_i + b_2 T_i^{\,2} , \\ C(T_i) &= c_0 + c_1 T_i + c_2 T_i^{\,2} + c_3 T_i^{\,3} + c_4 T_i^{\,4} . \end{aligned} \tag{B-12}$$

The coefficients b_j, c_j, and d_j obtained in this way are summarized in Table IX. The resultant differential cross section fits the data adequately; the shape of the angular distribution is nicely reproduced, and discrepancies, when they occur, appear in the normalization. This is probably not a fault of fitting but rather a fault in the data fitted: an absolute normalization is difficult to obtain in neutron experiments.

To estimate the error introduced by the Monte Carlo correction, we begin with Eq. (III-15):

$$y_m = \sum_{n=1}^{49} (A^{-1})_{mn} x_n . \tag{III-15}$$

The change in y_m due to an infinitesimal change dx_n in the variables

Table IX. Coefficients of fitting for n-p differential cross-section data.

Coefficient	Term in expansion				
	j=0 $\left(\frac{mb}{sr}\right)$	j=1 $\left(\frac{mb}{sr\text{-}MeV}\right)$	j=2 $\left(\frac{mb}{sr\text{-}MeV^2}\right)$	j=3 $\left(\frac{mb}{sr\text{-}MeV^3}\right)$	j=4 $\left(\frac{mb}{sr\text{-}MeV^4}\right)$
b_j	-0.302	-1.23×10^{-2}	4.49×10^{-5}	--	--
c_j	-0.899	0.211	-3.19×10^{-3}	1.35×10^{-5}	1.94×10^{-8}
d_j	339.6	861.4	-6.047	1.615×10^{-2}	--

x_n and a change dA_{ij} in the elements A_{ij} is given by

$$dy_m = \sum_{n=1}^{49} (A^{-1})_{nm}\, dx_n + \sum_{n=1}^{49}\sum_{i=1}^{49}\sum_{j=1}^{49} x_n \frac{\partial (A^{-1})_{mn}}{\partial A_{ij}}\, dA_{ij} \,. \qquad \text{(B-13)}$$

If we square this expression, we obtain

$$(dy_m)^2 = \sum_{n=1}^{49}\sum_{k=1}^{49} (A^{-1})_{mn}(A^{-1})_{mk}\, dx_n\, dx_k$$

$$+ 2 \sum_{n=1}^{49}\sum_{k=1}^{49}\sum_{i=1}^{49}\sum_{j=1}^{49} x_n (A^{-1})_{mk} \frac{\partial (A^{-1})_{mn}}{\partial A_{ij}}\, dA_{ij}\, dx_k$$

$$+ \sum_{n=1}^{49}\sum_{k=1}^{49}\sum_{i=1}^{49}\sum_{p=1}^{49}\sum_{j=1}^{49}\sum_{q=1}^{49} x_n x_k \frac{\partial (A^{-1})_{mn}}{\partial A_{ij}} \frac{\partial (A^{-1})_{mk}}{\partial A_{pq}}\, dA_{ij}\, dA_{pq} \,. \qquad \text{(B-14)}$$

An average is now taken over the independent variables x_n and A_{ij}; this property of independence allows us to write

$$\langle dx_n\, dA_{ij} \rangle = 0 \,,$$

$$\langle dx_n\, dx_k \rangle = \delta_{nk} (\Delta x_n)^2 \,,$$

and

$$\langle dA_{ij}\, dA_{pq} \rangle = \delta_{ip}\, \delta_{jq}\, (\Delta A_{ij})^2 \,, \qquad \text{(B-15)}$$

where δ_{mn} is the Kronecker delta:

$$\delta_{mn} = \begin{cases} 0, & m \neq n \\ 1, & m = n \end{cases} \,.$$

Using Eq. (B-15) to form this average, we find

$$(dy_m)^2 \equiv (\Delta y_m)^2$$

$$= \sum_{n=1}^{49} (A^{-1})_{mn}{}^2 (\Delta x_n)^2$$

$$+ \sum_{n=1}^{49} \sum_{i=1}^{49} \sum_{j=1}^{49} \left[x_n \frac{\partial (A^{-1})_{mn}}{\partial A_{ij}} \right]^2 (\Delta A_{ij})^2 . \qquad \text{(B-16)}$$

In performing the above average we have ignored the fact that Eq. (B-13) holds only for infinitesimal variations of the x_n and A_{ij}, since the averaging process involves integration of Eq. (B-14) weighted in accordance with the probability densities for these variables. Equation (B-16) is therefore approximate and holds only insofar as the probability densities for the x_n and the A_{ij} are sharply peaked about their means.

We may obtain an expression for

$$\frac{\partial (A^{-1})_{mn}}{\partial A_{ij}}$$

in terms of the $(A^{-1})_{mn}$ by differentiating the identity

$$\sum_{p=1}^{49} A_{kp} (A^{-1})_{pn} = \delta_{kn}$$

by A_{ij}:

$$\sum_{p=1}^{49} \frac{\partial A_{kp}}{\partial A_{ij}} (A^{-1})_{pn} + \sum_{p=1}^{49} A_{kp} \frac{\partial (A^{-1})_{pn}}{\partial A_{ij}} = 0 . \qquad \text{(B-17)}$$

But

$$\frac{\partial A_{kp}}{\partial A_{ij}} = \delta_{ik} \delta_{jp} , \qquad \text{(B-18)}$$

and we may write

$$\sum_{p=1}^{49} A_{kp} \frac{\partial (A^{-1})_{pn}}{\partial A_{ij}} = - \delta_{ik} (A^{-1})_{jn} . \qquad \text{(B-19)}$$

Multiplying by $(A^{-1})_{mk}$ and summing over k yield

$$\frac{\partial (A^{-1})_{mn}}{\partial A_{ij}} = \sum_{k=1}^{49} \sum_{p=1}^{49} (A^{-1})_{mk} A_{kp} \frac{\partial (A^{-1})_{kp}}{\partial A_{ij}}$$

$$= - \sum_{k=1}^{49} (A^{-1})_{mk} \delta_{ik} (A^{-1})_{jn}$$

$$= - (A^{-1})_{mi} (A^{-1})_{jn} , \qquad \text{(B-20)}$$

from which we obtain

$$(\Delta y_m)^2 = \sum_{n=1}^{49} (A^{-1})_{mn}^2 (\Delta x_n)^2 + \sum_{n=1}^{49} \sum_{i=1}^{49} \sum_{j=1}^{49} \left[(A^{-1})_{jn} x_n (A^{-1})_{mi} \Delta A_{ij} \right]^2$$

$$= \sum_{n=1}^{49} \left[(A^{-1})_{mn} \Delta x_n \right]^2 + \sum_{i=1}^{49} \sum_{j=1}^{49} \left[y_j (A^{-1})_{mi} \Delta A_{mi} \right]^2 , \qquad \text{(B-21)}$$

which is the expression quoted in Eq. (III-16) of the text.

- - - - - - - - - - -

This work was done under the auspices of the U. S. Atomic Energy Commission.

FOOTNOTES AND REFERENCES

1. G. F. Chew and F. E. Low, Phys. Rev. 113, 1640 (1959).
2. T. D. Lee and C. N. Yang, Nuovo Cimento 3, 749 (1956).
3. Hans A. Bethe and Frederic de Hoffman, Mesons and Fields (Row, Peterson, and Co., Evanston, Illinois, 1955), Vol. 2, p. 35 ff.
4. A. R. Erwin, R. March, W. D. Walker, and E. West, Phys. Rev. Letters 6, 628 (1961).
5. E. Pickup, D. K. Robinson, and E. O. Salant, Phys. Rev. Letters 7, 192 (1961).
6. J. Anderson, V. Bang, P. Burke, D. Carmony, and N. Schmitz, Phys. Rev. Letters 6, 365 (1961).
7. For details of the beam channel system see the Ph. D. Thesis of Joseph T. Lach, Effects of Single-Pion Exchange in the Reaction $p + p \rightarrow n + p + \pi^+$, University of California, (in preparation).
8. Owen Chamberlain, Ann. Rev. Nucl. Sci. 10, 161 (1960).
9. Ernest H. Rogers, Scattering of 310-MeV Positive Pions by Protons: Experiments and Analysis, Lawrence Radiation Laboratory Report UCRL-10127, March 1962 (unpublished).
10. A. E. Bjerke, Q. A. Kerns, and T. A. Nunamaker, Pulse Shaping and Standardizing of Photomultiplier Signals of Optimum Timing Information Using Tunnel Diodes, Lawrence Radiation Laboratory Report UCRL-9838, Sept. 1961 (unpublished).
11. In practice, the outputs of Array I were summed into four channels, each going to a separate Chronotron unit. For details of the procedure, see the material cited in reference 12.
12. For a detailed discussion of the electronics system, see Leonard B. Auerbach, Study of Pion-Pion Scattering from the Reaction $\pi^+ + p \rightarrow \pi^+ + \pi^+ + n$ at 1.25 and 1.75 BeV/c, (Ph. D. Thesis), UCRL-10530, Oct. 1962 (unpublished).
13. A. E. Bjerke, Q. A. Kerns, and T. A. Nunamaker, Nucl. Instr. Methods 12, 25 (1961).

14. Tom Innes and Quentin Kerns, Triggered Nanosecond Pulsed Light Source, Lawrence Radiation Laboratory Report UCRL-9726, Aug. 1961 (unpublished).

15. Paul G. Hoel, Introduction to Mathematical Statistics (John Wiley and Sons, Inc., New York, 1947), p. 70.

16. Clyde E. Wiegand, Tom Elioff, William B. Johnson, Leonard B. Auerbach, Joseph Lach, and Thomas Ypsilantis, Rev. Sci. Instr. 33, 526 (1962).

17. Wilmot N. Hess, Rev. Mod. Phys. 30, 368 (1958).

18. D. Kraus, K. Lande, E. Leboy, and W. Selove, Rev. Sci. Instr. 29, 1142 (1958).

19. Tom J. Ypsilantis, Experiments on Polarization in Nucleon-Nucleon Scattering at 310 MeV, University of California, Radiation Laboratory Report UCRL-3047, 1956.

20. For a description of the terminology and information content of magnetic tapes used as input for the IBM 709 Data Processing System, see IBM Reference Manual 709-7090 Data Processing System, Form A22-6503-1 (Nov. 1959).

21. A description of the FORTRAN Coding language may be found in IBM Reference Manual 709 FORTRAN Automatic Coding System, Form C28-6054-1 (March 1960); the FAP Coding language is summarized in many places, reference 20 for example.

22. Hoel, Mathematical Statistics, p. 134.

23. David V. Widder, Advanced Calculus (Prentice-Hall, Inc., New York, 1947), p. 205.

24. J. W. Cronin, R. Cool, and A. Abashian, Phys. Rev. 107, 1121 (1957).

25. N. Abbattista, M. Biasco, S. Mangelli, A. Romano, and P. Waloschek, Nuovo Cimento 23, 1 (1962).

26. I. Derado and N. Schmitz, Phys. Rev. 118, 309 (1960).

27. Werner Graeub, Lineare Algebra (Springer-Verlag, Berlin, 1958), p. 58.

28. Peter Cziffra and Michael J. Moravscik, A Practical Guide to the Method of Least Squares, Lawrence Radiation Laboratory Report UCRL-8523, (unpublished).

29. R. H. Dalitz, Phil. Mag. 44, 1068 (1953).

30. S. B. Treiman and C. N. Yang, Phys. Rev. Letters 8, 140 (1962).

31. Leonard B. Auerbach, Tom Elioff, William B. Johnson, Joseph Lach, Clyde E. Wiegand, and Thomas Ypsilantis, Phys. Rev. Letters 9, 173 (1962).

32. Widder, Advanced Calculus, p. 135.

33. Hans A. Bethe and Philip Morrison, Elementary Nuclear Theory (John Wiley and Sons, Inc., New York, 1956), p. 59.